THE DENSE MATTER EQUATION OF STATE FROM NEUTRON STAR RADIUS AND MASS MEASUREMENTS

Feryal Özel[1], Dimitrios Psaltis[1], Tolga Güver[2], Gordon Baym[3], Craig Heinke[4,6], and Sebastien Guillot[5]

[1] Department of Astronomy, University of Arizona, 933 N. Cherry Avenue, Tucson, AZ 85721, USA; fozel@email.arizona.edu
[2] Istanbul University, Science Faculty, Department of Astronomy and Space Sciences, Beyazit, 34119, Istanbul, Turkey
[3] Department of Physics, University of Illinois at Urbana-Champaign, 1110 W. Green Street, Urbana, IL 61801, USA
[4] Department of Physics, University of Alberta, CCIS 4-183, Edmonton, AB T6G 2E1, Canada
[5] Instituto de Astrofísica, Facultad de Física, Pontificia Universidad Católica de Chile, Av. Vicuña Mackenna 4860, 782-0436 Macul, Santiago, Chile

ABSTRACT

We present a comprehensive study of spectroscopic radius measurements of twelve neutron stars obtained during thermonuclear bursts or in quiescence. We incorporate, for the first time, a large number of systematic uncertainties in the measurement of the apparent angular sizes, Eddington fluxes, and distances, in the composition of the interstellar medium, and in the flux calibration of X-ray detectors. We also take into account the results of recent theoretical calculations of rotational effects on neutron star radii, of atmospheric effects on surface spectra, and of relativistic corrections to the Eddington critical flux. We employ Bayesian statistical frameworks to obtain neutron star radii from the spectroscopic measurements as well as to infer the equation of state from the radius measurements. Combining these with the results of experiments in the vicinity of nuclear saturation density and the observations of $\sim 2\,M_\odot$ neutron stars, we place strong and quantitative constraints on the properties of the equation of state between $\approx$2–8 times the nuclear saturation density. We find that around $M = 1.5\,M_\odot$, the preferred equation of state predicts radii between 10.1 and 11.1 km. When interpreting the pressure constraints in the context of high density equations of state based on interacting nucleons, our results suggest a relatively weak contribution of the three-body interaction potential.

Key words: dense matter – equation of state – stars: neutron – X-rays: binaries – X-rays: bursts – X-rays: stars

1. INTRODUCTION

The densest matter in the universe at low temperatures and at finite baryon density is found in the cores of neutron stars. Such conditions are not accessible to current laboratory experiments. Measuring the macroscopic properties of neutron stars, and in particular, their radii, offers the most direct and powerful probe of the composition of and interactions in cold, ultradense matter.

There has been a lot of recent progress in measuring neutron star radii with a variety of techniques and using them to constrain the equation of state (see Özel 2013 for a recent review). Spectroscopic observations of thermonuclear bursts from accreting neutron stars with the last generation of X-ray telescopes have provided measurements of both the radii and the masses of several sources with weakly correlated uncertainties (e.g., Özel et al. 2009, 2012a; Güver et al. 2010a, 2010b; Güver & Özel 2013). Observations of similar neutron stars during quiescence have yielded measurements of their apparent angular sizes, which leads to a determination of the radii with correlated uncertainties with the neutron star mass (Heinke et al. 2006, 2014; Webb & Barret 2007; Guillot et al. 2011, 2013).

A parallel avenue of progress has taken place in understanding the mapping from neutron star masses and radii to the equation of state. Several parametric representations of the equation of state allow radius measurements to be used for a direct inference of the pressure at several fiducial densities above the nuclear saturation density (ρ_{ns}; Lindblom 1992; Lattimer & Prakash 2001; Özel & Psaltis 2009; Read et al. 2009). Özel et al. (2010) used one of these mapping techniques on the radius measurements obtained from thermonuclear bursters to place the first constraints on the neutron star equation of state at high densities. They found that the relatively small observed radii point to lower pressures at and above $2\rho_{ns}$ than those predicted by purely nucleonic equations of state. Similarly, small radii were found by Guillot et al. (2013) in their analysis of quiescent neutron stars, which also point to softer equations of state than expected for nucleonic compositions. Steiner et al. (2010) and Lattimer & Steiner (2014a) found that substantial reinterpretation of the observed astrophysical phenomena and/or choosing extreme values for some of the measurements was needed to make the observed radii larger and reduce the tension with the predictions of some nucleonic equations of state.

Since these first studies, our understanding of systematics in the spectroscopic measurements has been substantially improved and theoretical work has identified a number of small, albeit important, corrections that need to be applied to the inference of neutron star radii. In this paper, we incorporate these corrections and sources of uncertainty in the analysis of the spectroscopic data and infer the parameters of the neutron star matter equation of state that are consistent with all astrophysical data as well as with laboratory experiments at low densities.

Specifically, comprehensive studies of a large sample of sources allowed for a quantitative assessment of the systematic uncertainties in the spectroscopic measurements. For thermonuclear bursters, a Bayesian mixture technique with an outlier detection scheme was applied on a very large *Rossi X-ray Timing Explorer* (*RXTE*) sample consisting of 13,095 burst spectra from 12 sources. This resulted in a data-driven measurement of the intrinsic scatter in the apparent angular sizes during the cooling tails of bursts

---

[6] Alexander von Humboldt Fellow, at Max-Planck-Institut für Radioastronomie, Auf dem Hügel 69, D-53121 Bonn, Germany.

(Güver et al. 2012b) and of the scatter in the touchdown fluxes during photospheric radius-expansion bursts in individual sources (Güver et al. 2012a). Moreover, a comparison of the simultaneous observations of bursts with multiple X-ray instruments, and specifically between the Proportional Counter Array (PCA) and *Chandra* ACIS significantly constrained any biases in the *RXTE* burst fluxes due to calibration to $\lesssim 1\%$ (Güver et al. 2015). For quiescent neutron stars, long observations with *Chandra* and *XMM-Newton* resulted in high signal-to-noise spectra, which, in combination with explorations of uncertainties in the atmospheric composition and the amount of interstellar extinction in the soft X-rays, improved the inferences of their apparent angular sizes (Guillot et al. 2013; Guillot & Rutledge 2014; Heinke et al. 2014).

Numerous developments have also taken place on the theoretical models that are employed to interpret these observational data. Since most of the X-ray burst sources spin at moderately high rates, general relativistic corrections to the apparent angular sizes that go beyond the Schwarzschild approximation and incorporate effects that are of second order in spin have been calculated (Bauböck et al. 2012, 2015). Radiative equilibrium models of neutron star atmospheres have also been improved by including the angle and energy dependence of the scattering kernels (Suleimanov et al. 2011, 2012). These resulted in more accurate relations between spectral and effective temperatures, as well as in notable temperature corrections to the Eddington (touchdown) fluxes. Different statistical tools for inferring the uncertainties in the neutron star radii and masses from burst data have been assessed. This led to the identification of a Bayesian method that does not introduce biases in the radius measurements, in contrast to the frequentist method used in earlier studies (see the companion paper Özel & Psaltis 2015). Finally, Bayesian methods have also been developed to infer the properties of the dense matter equation of state from radius and mass measurements (Steiner et al. 2010).

There are additional astrophysical data and laboratory experiments that can be used in conjunction with the neutron star radius measurements to further constrain the equation of state of dense matter. In this paper, we use the results of nucleon–nucleon interaction calculations that are firmly based on scattering data below 350 MeV and the properties of light nuclei (Akmal et al. 1998; Pieper et al. 2001; Gandolfi et al. 2012) to place a lower limit on the pressure of neutron-rich matter at densities $\sim 2\rho_{\rm ns}$, where $\rho_{\rm ns}$ is the nuclear matter saturation density, $\sim 2.7 \times 10^{14}\,{\rm g\,cm^{-3}}$ (or $n_{\rm ns} \sim 0.16\,{\rm fm^{-3}}$). We also use the observations of the two neutron stars with the highest measured masses (Demorest et al. 2010; Antoniadis et al. 2013) to exclude the regions of the pressure parameter space that do not produce $\sim 2\,M_\odot$ neutron stars.

In Section 2, we introduce the improved theoretical models for the rotational corrections to the apparent angular sizes, the temperature corrections to the inferred Eddington limit, and the Bayesian framework for combining these two measurements. In Section 3, we present the spectroscopic data as well as the inferred radii for each of the 12 sources included in this study. In Section 4, we obtain constraints on the neutron star radius and a mono-parametric equation of state by combining all of the individual radius measurements. In Section 5, we use a Bayesian technique to map the measured radii and masses into the pressures at three fiducial densities, taking into account the additional astrophysical and laboratory constraints. Finally, in Section 6, we discuss the implications of our findings for neutron star astrophysics and nuclear models.

2. THEORETICAL FRAMEWORK FOR SPECTROSCOPIC NEUTRON STAR RADIUS MEASUREMENTS

2.1. Rotational Corrections to the Apparent Angular Size

For neutron stars that show thermonuclear bursts or that are in quiescence, the measurements of the radii rely on the detection of thermal emission from their surfaces. For such compact sources, the ratio $F/\sigma_{\rm B} T_{\rm c}^4$, where F is the observed thermal flux, $\sigma_{\rm B}$ is the Stefan–Boltzmann constant, and $T_{\rm c}$ is the temperature measured from the spectrum, yields the apparent angular size A_∞ of the source. For slowly spinning neutron stars, this relates to the stellar radius R via

$$A_\infty = \frac{R^2}{D^2 f_c^4}\left(1 - \frac{2GM}{Rc^2}\right)^{-1}, \tag{1}$$

where M is the mass of the neutron star, D is its distance, f_c is the color correction factor that takes into account the distortions in the spectrum due to the stellar atmosphere, G is the gravitational constant, and c is the speed of light.

All neutron stars with measured spin frequencies in our sample spin at frequencies that are larger than 400 Hz. At such frequencies, the Doppler broadening of the spectrum, as well as distortions related to the oblateness and the quadrupole moment of the neutron star, become important. Bauböck et al. (2015) explored these effects in detail and devised an approximate formula for the spin corrections to the apparent surface area. In the absence of any additional information on the inclination of the source, the appropriately weighted angular size for a spin frequency $f_{\rm NS}$ becomes

$$A_\infty = \frac{R^2}{D^2 f_c^4}\left(1 - \frac{2GM}{Rc^2}\right)^{-1}$$
$$\times \left\{1 + \left[\left(0.108 - 0.096\frac{M}{M_\odot}\right) + \left(-0.061 + 0.114\frac{M}{M_\odot}\right)\frac{R}{10\,{\rm km}} - 0.128\left(\frac{R}{10\,{\rm km}}\right)^2\right]\left(\frac{f_{\rm NS}}{1000\,{\rm Hz}}\right)^2\right\}^2. \tag{2}$$

In Figure 1, we show in blue the contour of constant apparent angular size on the mass–radius plane for a $M = 1.4\,M_\odot$ and $R = 10\,{\rm km}$ neutron star spinning at 600 Hz. To highlight the effect of the rotational corrections, we also plot in red the corresponding contour obtained under the Schwarzschild approximation used in the previous studies. As discussed in Bauböck et al. (2015), the rotational effects lead to larger angular sizes for the same neutron star mass and radius.
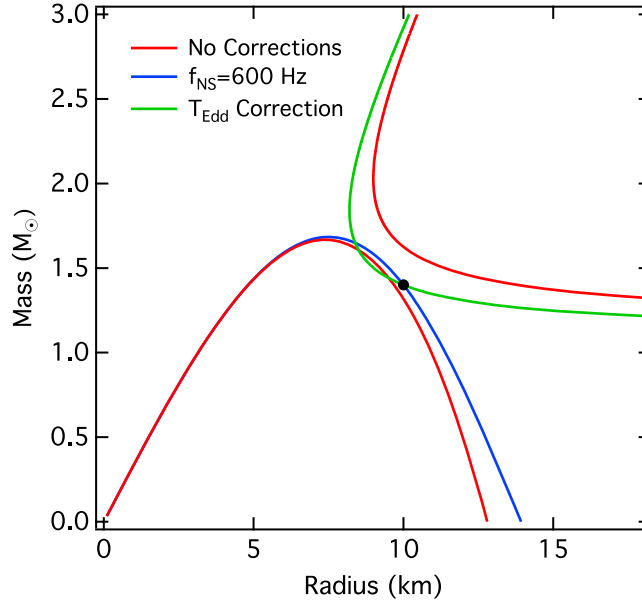
Figure 1. Contours of constant apparent angular size (blue) and touchdown flux (green) for an $M = 1.4\,M_\odot$ and $R = 10$ km neutron star spinning at 600 Hz and a spectral temperature during the touchdown moment of Eddington limited bursts calculated using Equation (8) for this mass and radius. These curves include the corrections to the apparent area due to neutron star spin and the temperature correction to the Eddington limit, respectively. The red curves are the corresponding contours when these corrections are not taken into account and would have led to no solutions for the neutron star mass and radius.

2.2. Temperature Corrections to the Eddington Limit

The atmospheres of neutron stars during thermonuclear bursts are dominated by electron scattering. During strong bursts, the radiation forces lift the photosphere above the neutron star surface and allow for a measurement of the Eddington critical luminosity. When this luminosity is measured at the touchdown point, i.e., when the photosphere has returned to the neutron star surface, it is related to the neutron star mass and radius via

$$F_{\rm td} = \frac{GMc}{k_{\rm es}D^2}\left(1 - \frac{2GM}{Rc^2}\right)^{1/2},\tag{3}$$

where

$$k_{\rm es} \equiv 0.2(1 + X)\ {\rm cm}^2\,{\rm g}^{-1}\tag{4}$$

is the electron scattering opacity and X is the hydrogen mass fraction of the atmosphere.

Because of the energy dependence in the Klein–Nishina cross section and the fact that the photons exchange energy with the electrons at each scattering, the Eddington flux depends on the temperature of the atmosphere. Paczynski (1983) derived an approximation for this temperature correction, which was further refined by Suleimanov et al. (2012), by taking into account the angular dependence of the scattering processes. With the approximate formula given in the latter study, the Eddington flux becomes

$$F_{\rm td} = \frac{GMc}{k_{\rm es}D^2}\left(1 - \frac{2GM}{Rc^2}\right)^{1/2}\left[1 + \left(\frac{kT_c}{38.8\ {\rm keV}}\right)^{a_g}\left(1 - \frac{2GM}{Rc^2}\right)^{-a_g/2}\right],\tag{5}$$

where

$$a_g = 1.01 + 0.067\log\left(\frac{g_{\rm eff}}{10^{14}\ {\rm cm\,s}^{-2}}\right)\tag{6}$$

and

$$g_{\rm eff} = \frac{GM}{R^2}\left(1 - \frac{2GM}{Rc^2}\right)^{-1/2}.\tag{7}$$

In Equation (5), the correction to the Eddington flux depends on the color temperature when the atmosphere reaches that limit, and this color temperature in turn depends on the mass and radius of the neutron star and the composition of the atmosphere via

$$T_{\rm Edd,c} = f_c\,T_{\rm Edd,eff} = f_c\left(\frac{g_{\rm eff}c}{\sigma_{\rm B}k_{\rm es}}\right)^{1/4} = f_c\left(\frac{GMc}{\sigma_{\rm B}k_{\rm es}R^2}\right)^{1/4}\left(1 - \frac{2GM}{Rc^2}\right)^{-1/8},\tag{8}$$
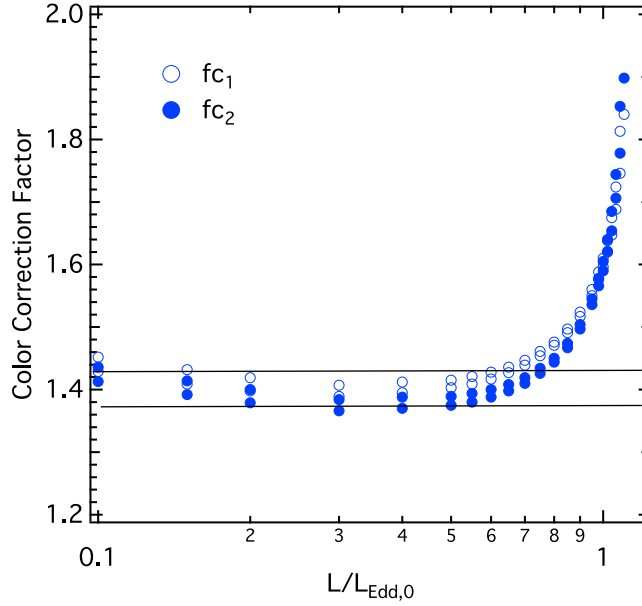
where $\sigma_{\rm B}$ is the Boltzmann constant.

Figure 2. Color correction factors from the models of He-rich neutron-star atmospheres by Suleimanov et al. (2012) for effective gravitational accelerations in the range $\log g_{\rm eff} = 14.3$–14.6. The open and filled circles correspond to two different definitions of the color-correction factor explored by Suleimanov et al. (2012). The two horizontal lines show the range of values we use in this paper, which accurately reproduces the model results for fluxes less than about 0.7 of the critical Eddington flux.

In Figure 1, we show in green the contour of constant touchdown flux in the mass–radius plane for a $M = 1.4\,M_\odot$ and $R = 10\,\mathrm{km}$ neutron star with hydrogen mass fraction $X = 0$ and a color correction factor at touchdown of $f_c = 1.9$. We also plot in red the corresponding contour obtained when the temperature correction to the Eddington flux is not taken into account, as was done in the previous studies. Because at high temperatures the scaterring cross section decreases, a measured Eddington flux corresponds to a smaller mass (and radius).

2.3. Statistics of Combining Observables to Infer Neutron Star Radii

It is clear from Equations (2) and (5) that measurements of the apparent angular size and the Eddington flux of a neutron star can be combined to determine its mass when the distance to the source is known. In earlier studies, this inference was performed and the uncertainties were assessed in a frequentist approach. We showed in a companion paper that this approach suffers from significant biases for the range of masses and radii expected for neutron stars (see Özel & Psaltis 2015a). To alleviate these shortcomings, we devised a Bayesian framework that more faithfully reconstructs masses and radii from synthetic data and we utilize it in the present analysis.

Using Bayes' theorem, we write the likelihood $P(M, R \mid \text{data})$ that a neutron star has a given mass and radius given a set of spectroscopic observables as

$$P(M, R \mid \text{data}) = CP(\text{data} \mid M, R)P_{\rm pri}(M)P_{\rm pri}(R), \qquad (9)$$

where $P_{\rm pri}(M)$ and $P_{\rm pri}(R)$ are the priors over the mass and radius, and C is an appropriate normalization constant. Given that A and $F_{\rm td}$ are ideally uncorrelated measurements, we can write

$$P(\text{data} \mid M, R) = \int P(D)\, dD \int P(f_c)\, df_c \int P(X)\, dX \int P(f_{\rm NS})\, df_{\rm NS}$$
$$\times\, P[F_{\rm td}(M, R, D, X)]\, P[A(M, R, D, f_{\rm NS}, f_c)]. \qquad (10)$$

Here, $P(D)$, $P(F_{\rm td})$, and $P(A)$ are the posterior likelihoods of the measurements over the distance, the touchdown flux, and the apparent angular size; $P(X)$, $P(f_c)$, and $P(f_{\rm NS})$ are the priors over the hydrogen mass fraction, the color correction factor, and the spin frequency of the neutron star, respectively. Hereafter, when we use this expression, we assume flat priors over the mass between 0.6 and 3.5 $M_\odot$ and over the radius between the Schwarzschild radius that corresponds to each mass and 20 km. These ranges are chosen to be large enough such that their precise values do not affect the posterior likelihoods.

When the spin frequency of a source is previously measured, we take as $P(f_{\rm NS})$ a delta function at the known frequency. When the spin frequency is not known, we assume a flat prior between 250 and 650 Hz, which is consistent with the range of spins observed in thermonuclear bursters, and apply spin corrections to the apparent angular size with this prior.

2.4. The Spectra of Thermonuclear Bursters

In order to obtain the mass–radius contours of a neutron star from the measurement of its apparent angular size via Equation (2), we need to employ models of the neutron star atmosphere that enter through the color correction factor f_c. Since the initial work of

Table 1
Properties of Neutron Star Burst Sources

Source	App. Angular Size (km/10 kpc)^2	Touchdown Flux[a] (10^{-8} erg s^{-1} cm^{-2})	Spin Freq.[b] (Hz)	Distance[b] (kpc)	Radius[c] (km)
4U 1820−30	89.9 ± 15.9	5.98 ± 0.66	⋯	7.6 ± 0.4 (4) or 8.4 ± 0.6 (5), (6)	11.1 ± 1.8
SAX J1748.9−2021	89.7 ± 9.6	4.03 ± 0.54	410 (1)	8.2 ± 0.6 (4), (5), (7)	11.7 ± 1.7
EXO 1745−248	117.8 ± 19.9	6.69 ± 0.74	⋯	6.3; ΔD = 0.63 (8), (9)	10.5 ± 1.6
KS 1731−260	96.0 ± 7.9	4.71 ± 0.52	524 (2)	∼7–9 (10)	10.0 ± 2.2
4U 1724−207	113.8 ± 15.4	5.29 ± 0.58	⋯	7.4 ± 0.5	12.2 ± 1.4
4U 1608−52	314 ± 44.3	18.5 ± 2.0	620 (3)	See the Appendix	9.8 ± 1.8

Notes.
[a] A minimum systematic uncertainty of 11% has been assigned in accordance with Güver et al. (2012a).
[b] References: (1) Altamirano et al. (2008), (2) Smith et al. (1997), (3) Hartman et al. (2003), (4) Kuulkers et al. (2003), (5) Valenti et al. (2007), (6) Güver et al. (2010b), (7) Güver & Özel (2013), (8) Ortolani et al. (2007), (9) Özel et al. (2009), (10) Özel et al. (2012a).
[c] The radius and its 68% uncertainty obtained by marginalizing the mass–radius likelihood of each source over the observed mass distribution, as in Figure 12.

London et al. (1986) increasingly more sophisticated calculations have been performed for a variety of compositions and effective gravitational accelerations (Madej et al. 2004; Majczyna et al. 2005; Suleimanov et al. 2011). Most recently, Suleimanov et al. (2012) calculated a large set of models, taking into account the full angular and energy dependence of the scattering process. They found that, for fluxes between ≈0.1–0.7 of the Eddington critical flux, which is the range that we consider here, the color correction factors depend very weakly on the effective gravitational acceleration or on the particular definition of the color correction factor and are approximately constant in the range 1.4 ± 0.05 (see Figure 2). Note that the color correction factors do evolve significantly at very high and very low flux levels, which we exclude when measuring neutron star apparent angular sizes during the cooling tails of thermonuclear bursts (see Güver et al. 2012b). In the remainder of this paper, we consider a flat prior distribution of the color correction factor in the above range (see Equation (10)).

3. OBSERVATIONS AND RADIUS MEASUREMENTS OF INDIVIDUAL SOURCES

3.1. Thermonuclear Bursters

There are five sources for which thermonuclear burst data have been previously used to measure neutron star radii using their apparent angular sizes, touchdown fluxes, and distances (see Table 1).

We also include in the present analysis 4U 1724−307, for which Suleimanov et al. (2011) reported a radius measurement based on the spectral evolution during the cooling tail of one long burst observed from this source. As discussed in Güver et al. (2012b), the spectra from that long burst used in the Suleimanov et al. (2011) study are significantly different from blackbodies and from model atmosphere spectra, resulting in χ^2/dof in the range 1–8 in the spectral fits (see also in't Zand & Weinberg 2010). This indicates significant contamination of the surface emission, either by the accretion flow or by atomic lines from the ashes of the burst that have been brought up to the photosphere, which makes the results unreliable. Instead, we make use of the cooling tails of the two normal bursts observed from 4U 1724−207 to determine the apparent angular size (see Güver et al. 2012b). The spectra from these two bursts show the expected thermal shape and result in acceptable values for χ^2/dof. We also make use of the touchdown flux measured from these bursts (Güver et al. 2012a) when determining the neutron star radius.

Since the earliest measurements, Güver et al. (2012a, 2012b), conducted studies on the entire *RXTE* burst data set and found ∼10% systematic uncertainties in the apparent angular sizes and the touchdown fluxes in the most prolific bursters. In addition, Güver et al. (2015) placed an upper limit of ∼1% on the systematic differences in the flux calibration between *RXTE* and *Chandra*, which, in principle, can affect the measured burst fluxes.

We reanalyze the data on these six sources uniformly, following the procedures used and described in Güver et al. (2012a, 2012b). Specifically, (i) we apply the appropriate deadtime correction to the observed countrates, which leads to a small increase in the angular sizes and touchdown fluxes for the brightest sources. (ii) We employ a Bayesian Gaussian-mixture model to quantify the intrinsic scatter in the measurements of the angular sizes and the touchdown fluxes. This is typically larger than the formal uncertainties in the measurements and increases the uncertainties in the inferred radii. (iii) When the number of Eddington-limited bursts of an individual source is too small to assess the scatter in the touchdown flux, we take an 11% systematic uncertainty in this quantity following the analysis of Güver et al. (2012a) on the sample of sources with limited number of bursts. (iv) We add an uncertainty of 1% in the apparent angular sizes and the touchdown fluxes to account for the flux calibration uncertainties. We summarize all the measurements in Table 1 and discuss the additional details of the source distances and atmospheric compositions for individual sources below. Note that the uncertainties in Table 1 do not include the 1% flux calibration uncertainties, which we add in quadrature when inferring the radii. We also list the ID numbers of the bursts used in this study in Table 4 of the Appendix, following the numbering system used in Galloway et al. (2008a).

3.1.1. 4U 1820−30

4U 1820−30 is an ultracompact binary in the metal-rich globular cluster NGC 6624. Güver et al. (2010b) discussed two distance measurements performed in the optical (Kuulkers et al. 2003) and in the near-IR bands (Valenti et al. 2007). The first gives a distance of 7.6 ± 0.4 kpc and the second gives 8.4 ± 0.6 kpc. Harris (1996) and Harris (2010 revision) found a compatible distance estimate
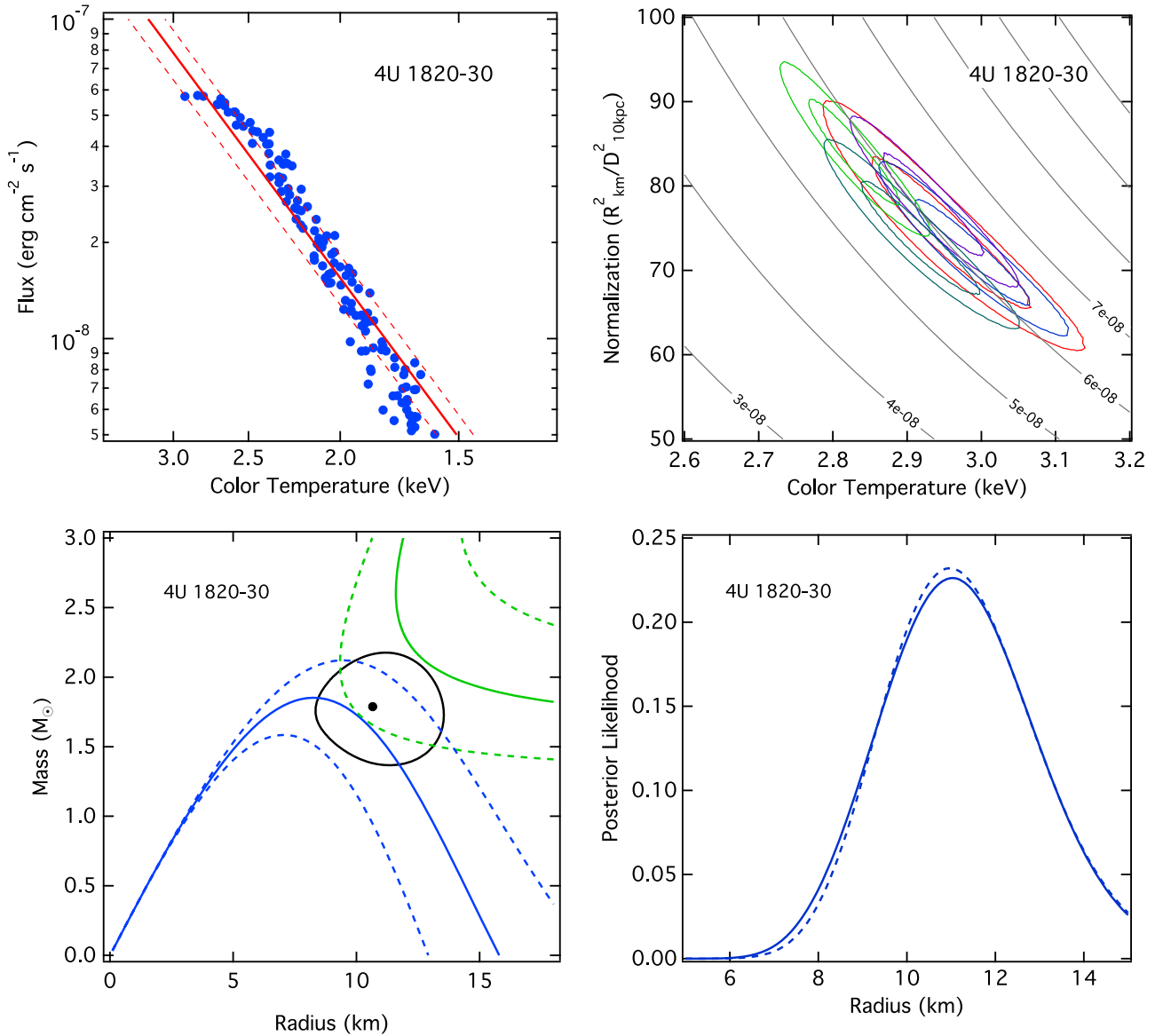
Figure 3. (Top left) The evolution of the flux and temperature measured for all the spectra in the cooling tails of bursts from 4U 1820−30. The diagonal red lines show the best-fit blackbody normalization and its 1σ uncertainty. (Top right) The 1σ and 2σ confidence contours over the blackbody normalization and temperature measured at the touchdown moment in the PRE bursts. The black diagonal lines correspond to contours of constant touchdown flux. (Bottom left) The black solid curve shows the 68% confidence contour over the mass and radius of 4U 1820−30 obtained by combining all the measurements and priors; the filled circle marks the location of the highest likelihood. The solid blue and green lines denote the mass–radius curves obtained from the most likely values of the apparent angular size and Eddington flux, respectively, while the dashed curves denote the 1σ uncertainties of these measurements. (Bottom right) The posterior likelihood over the neutron star radius after the two-dimensional likelihoods are marginalized over mass. The dashed line assumes a flat prior over mass, while the solid line assumes as a prior the observationally inferred mass distribution of recycled pulsars, as discussed in the text.

of 7.9 kpc in the optical band, with an uncertainty of 0.4 kpc.[7] Without any further information to choose between the optical and the near-IR measurements, Güver et al. (2010b) combined them into a single boxcar likelihood between 6.8 and 9.6 kpc, which placed more than warranted likelihoods at the shortest and intermediate distances. Here, we instead opt to use a double Gaussian likelihood with means and standard deviations that reflect the individual measurements of Kuulkers et al. (2003) and Valenti et al. (2007) and give equal integrated likelihood to each.

The fact that the neutron star is in a 11.4 minute binary (Stella et al. 1987) requires that it is fed by a degenerate dwarf companion that is free of hydrogen. For this reason, when inferring the radii, we set the hydrogen abundance to $X = 0$. No burst oscillations or persistent pulsations have been observed from this source. Because of this, when applying spin corrections to the apparent angular size, we assume a flat prior in spin between 250 and 650 Hz, as discussed in Section 2.3.

The top left panel of Figure 3 shows the evolution of the flux and temperature during the cooling tails of five bursts observed from 4U 1820−30, while the top right panel shows the 68% and 95% confidence contours in the measurement of the blackbody

---

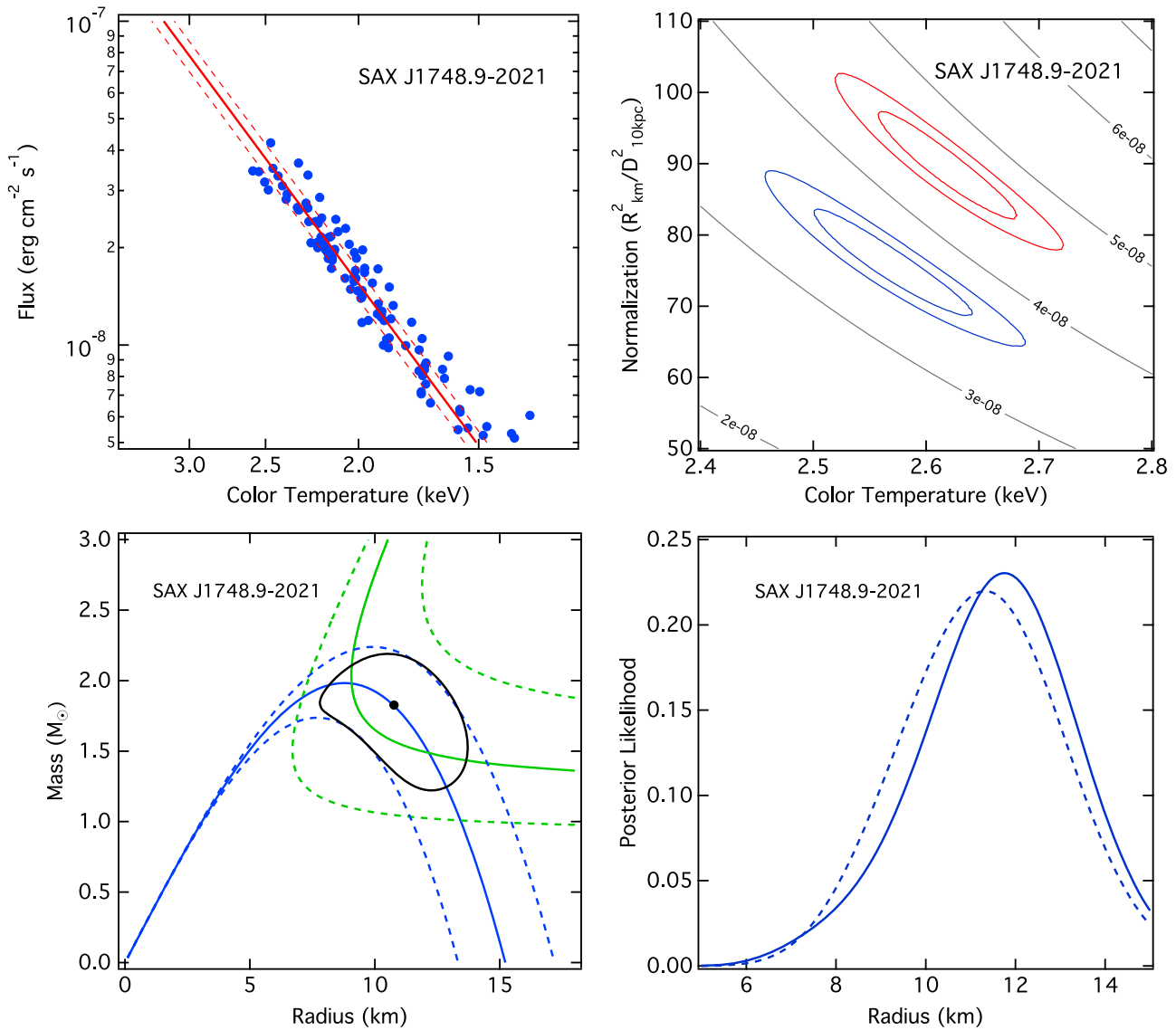[7] See http://physwww.physics.mcmaster.ca/~harris/mwgc.ref

Figure 4. Same as in Figure 3 but for SAX J1748.9−2021.

normalization versus temperature during the touchdown phases in the five Eddington-limited bursts. Because the intrinsic scatter in the touchdown flux of this source is very small, we assign an 11% uncertainty to this measurement as discussed above.

The lower left panel shows the 68% and 95% confidence contours over the mass and radius of 4U 1820−30 inferred within the Bayesian framework discussed in Section 2.3, along with the contours of constant apparent angular size (blue) and touchdown flux (green) obtained for this source. The lower right panel shows the likelihood over the radius when we marginalized the two-dimensional likelihood over mass. We do this for a flat prior on mass between 0 and 3 $M_\odot$, as well as for the observed mass distribution of fast radio pulsars, which are the descendants of the low-mass X-ray binaries that make up our sample. As discussed in Özel et al. (2012b), the latter mass distribution can be represented by a Gaussian with a mean of 1.46 $M_\odot$ and a dispersion of 0.21$M_\odot$. The difference in the result between using the two different priors over the mass is minor. (Note that we use the full two-dimensional likelihoods without these observational priors on mass when inferring the parameters of the equation of state.)

3.1.2. SAX J1748.9−2021

The transient neutron star X-ray binary SAX J1748.9−2021 is located in the globular cluster NGC 6440, which is a massive and old cluster in the Galactic bulge. Two optical studies and one near-IR study give consistent and well-constrained distances to NGC 6440: Kuulkers et al. (2003) reported $8.4^{+1.5}_{-1.3}$ kpc, Harris (1996) found 8.5 kpc, while Valenti et al. (2007) found 8.2 ± 0.6 kpc using near-IR data. In this last study, the distance uncertainty is improved and takes into account the systematic errors introduced by the method of comparing the properties of NGC 6440, including its metallicity and age, to the reference cluster. Because the central values of the two measurements differ by less than the 1σ uncertainty for either, here we adopt the latter distance and its uncertainty.

SAX J1748.9−2021 has a spin frequency of 420 Hz, detected during intermittent pulsations observed in the persistent emission (Altamirano et al. 2008). The same study also found a binary orbital period of 8.7 hr. Because there is no specific information about the evolutionary state of the donor, we take a flat prior in the hydrogen mass fraction between 0 and 0.7.

The top left panel of Figure 4 shows the evolution of the flux and temperature during the cooling tails of four bursts observed from SAX J1748.9−2021, while the top right panel shows the 68% and 95% confidence contours in the measurement of the blackbody normalization versus temperature during the touchdown phases in its two Eddington-limited bursts.

The lower panels of Figure 4 show the 68% confidence contour in mass and radius as well as the posterior likelihood marginalized over mass using the Bayesian framework and priors discussed above.

3.1.3. EXO 1745−248

EXO 1745−248 is located in Terzan 5, one of the most metal-rich globular clusters in the Galaxy. The distance to Terzan 5 was obtained using *Hubble Space Telescope* (*HST*)/NICMOS data (Ortolani et al. 2007). The sources of uncertainty in the distance measurement were discussed in detail in Özel et al. (2009). Here we adopt the same flat likelihood over distance centered at 6.3 kpc, with a width of 0.63 kpc.

No burst oscillations or persistent pulsations have ever been observed from EXO 1745−248. As before, we adopt a flat prior over its spin frequency between 250 and 650 Hz when calculating the spin corrections to the apparent angular size. The nature of the companion of EXO 1745−248 is ambiguous (Heinke et al. 2003). While the empirical comparison of its spectrum to those of ultracompact sources suggested an ultracompact binary with a hydrogen-poor companion, the identification of a possible infrared counterpart leaves open the possibility of a hydrogen-rich donor. To account for both possibilities, we take a flat prior over the hydrogen mass fraction in the range $X = 0$–0.7.

The top panels of Figure 5 show the evolution of the flux and temperature during the cooling tails of two bursts (left) and the 68% and 95% confidence contours in the measurement of the blackbody normalization versus temperature during the touchdown phases of these two Eddington-limited bursts (right).

The lower panels of Figure 5 show, as before, the 68% confidence contour in mass and radius (left) derived in the Bayesian framework from the measurements of the apparent angular size, touchdown flux, and the distance, as well as the posterior likelihood marginalized over mass (right).

3.1.4. KS 1731−260

KS 1731−260 is a binary in the Galactic bulge, lying in the direction of Baade's window. Özel et al. (2012a) derived a distance prior to this source based on the stellar density along the line of sight. We use the same numerical prior in the current study, which places KS 1731−260 at a distance of approximately 7−9 kpc.

KS 1731−260 has a spin frequency of 524 Hz based on the detection of burst oscillations (Smith et al. 1997). Its optical counterpart has been identified (Zurita et al. 2010) and the duration and the energetics of some of its X-ray bursts point to accreted fuel that is hydrogen-rich. Nevertheless, because there is no conclusive evidence on the hydrogen content of the bursts we analyze here, we allow for a flat distribution in the hydrogen mass fraction X between 0 and 0.7.

We show in the top panels of Figure 6 the flux versus temperature observed during the cooling tails of 24 X-ray bursts used for the measurement of the apparent angular size and the 68% and 95% confidence contours in the blackbody normalization and temperature measured during the touchdown phases of two Eddington limited bursts.

The lower left panel of Figure 6 shows the 68% confidence contours over the mass and radius of KS 1731−260, inferred within the Bayesian framework, along with the contours of constant apparent angular size (blue) and touchdown flux (green) obtained for this source. The lower right panel shows the likelihood over the radius when we marginalized the two-dimensional likelihood over mass.

3.1.5. 4U 1724−207

4U 1724−207 lies in the globular cluster Terzan 2. Early studies of the distance to this cluster by Ortolani et al. (2007) obtained a distance of 5.3 or 7.7 kpc, depending on whether the selective extinction, R, was set to 3.1 or 3.6. The most recent study by Valenti et al. (2010) used near-IR observations of red giant branch stars and led to a distance of 7.4 kpc. Independent of the reddening or color–magnitude measurements, one can statistically argue that the distance of Terzan 2 should be the same as the distance to the Galactic center (Racine & Harris 1989). This is because the whole system of globular clusters is centrally concentrated around the Galactic center, and given the fact that the direction of Terzan 2 is within the Galactic bulge region, it is likely that its distance is close to 8.0 kpc (Reid 1993). Based on these arguments and in order to avoid using a measurement that strongly depends on the assumed extinction, we adopt the recent measurement of Valenti et al. (2010) of 7.4 ± 0.5 kpc. The error primarily reflects the systematic uncertainty in the measurements of the distances to globular clusters, as estimated by using 47 Tuc as a reference.

There have been no studies on the composition of the companion to 4U 1724−207 and no detected burst oscillations or persistent pulsations from this source. For this reason, when inferring its radius, we use a flat distribution in hydrogen abundance between $X = 0$ and $X = 0.7$ and a flat distribution in spin frequency between 250 and 650 Hz.

In the top left panel of Figure 7, we show the flux versus temperature diagram during the cooling tails of the bursts for which the blackbody model provides an acceptable fit to the data (see discussion in Güver et al. 2010b). In the top right panel, we show the 68% and 95% confidence contours in the measured blackbody normalization versus temperature during the touchdown phases of two Eddington-limited bursts. Finally, in the lower two panels of the same figure, we show (left) the 65% confidence contours in the
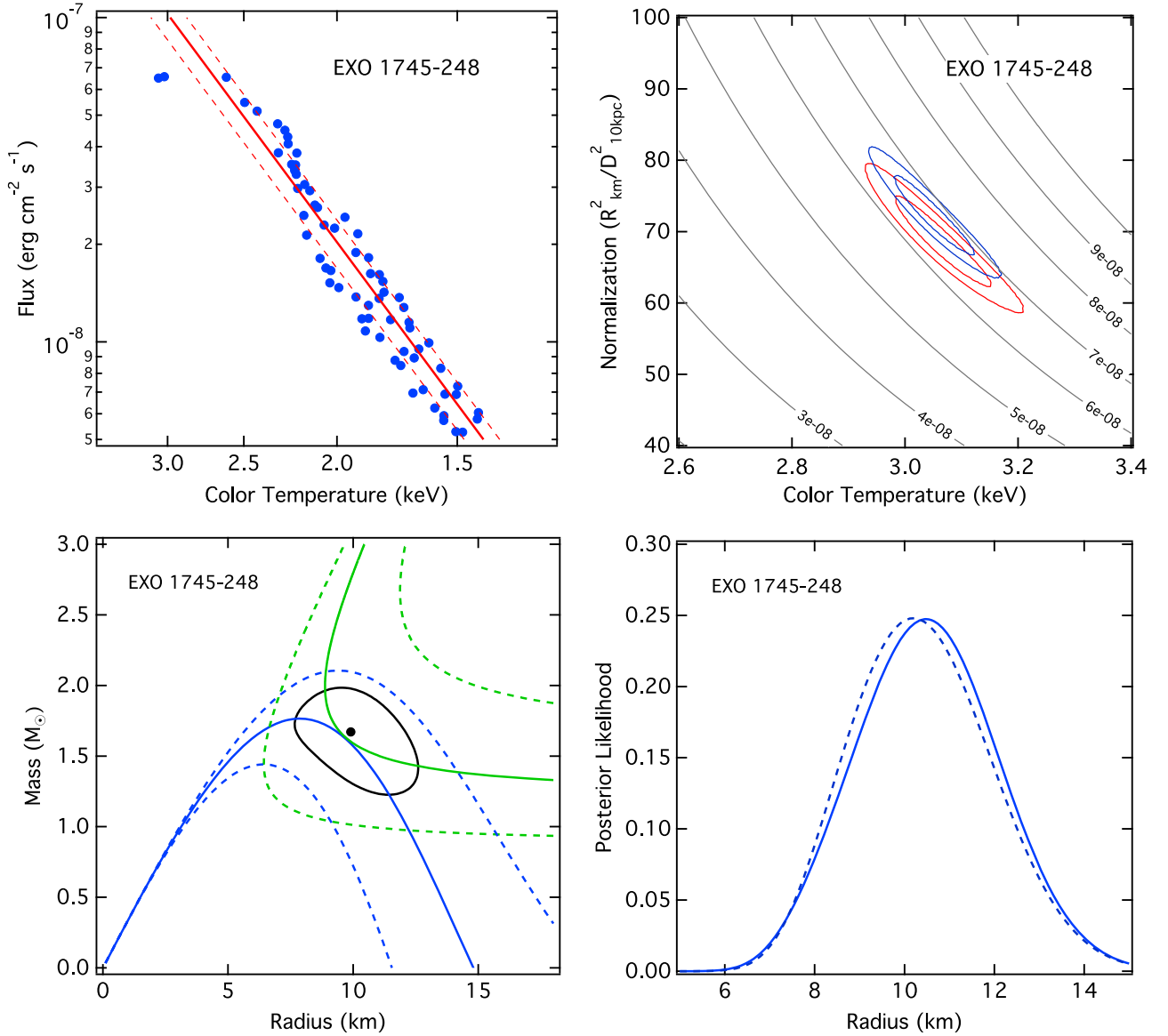
Figure 5. Same as in Figure 3 but for EXO 1745−248.

inferred mass and radius of 4U 1724−207 and (right) the posterior likelihood over radius, after we marginalize over the mass of the neutron star.

3.1.6. 4U 1608−52

4U 1608−52 lies in the Galactic disk. The distance to this source was measured in Güver et al. (2010a) by comparing the extinction obtained from the red clump stars along the line of sight to the extinction to the binary inferred from the high energy-resolution X-ray observations. We repeat this analysis in the Appendix, utilizing a new *Chandra* observation and the latest relation between the optical extinction A_V and the hydrogen column density N_H obtained in a new study (Foight et al. 2015). The new results place a lower limit of 3 kpc on the distance and give the highest likelihood at ∼4 kpc.

4U 1608−52 is the fastest spinning source in the current sample, with a spin frequency of 620 Hz (Hartman et al. 2003). As with the other sources whose companions do not have known compositions, we take a boxcar prior for the hydrogen mass fraction between $X = 0$ and $X = 0.7$.

In Güver et al. (2012b), we developed a Bayesian Gaussian-mixture method for outlier detection and measurement of the systematic uncertainties in the apparent angular size during the cooling tails of the bursts. 4U 1608−52 is the only source in the present sample for which such outliers were detected in the observed bursts. We discuss these in the Appendix. The top left panel of Figure 8 uses different color symbols to distinguish the main sequence of the cooling tail from these outliers.

The upper right panel in the same figure shows the confidence contours in the blackbody normalization and temperature in the touchdown moments of the three Eddington limited bursts, which include the newly detected burst during the simultaneous *RXTE*
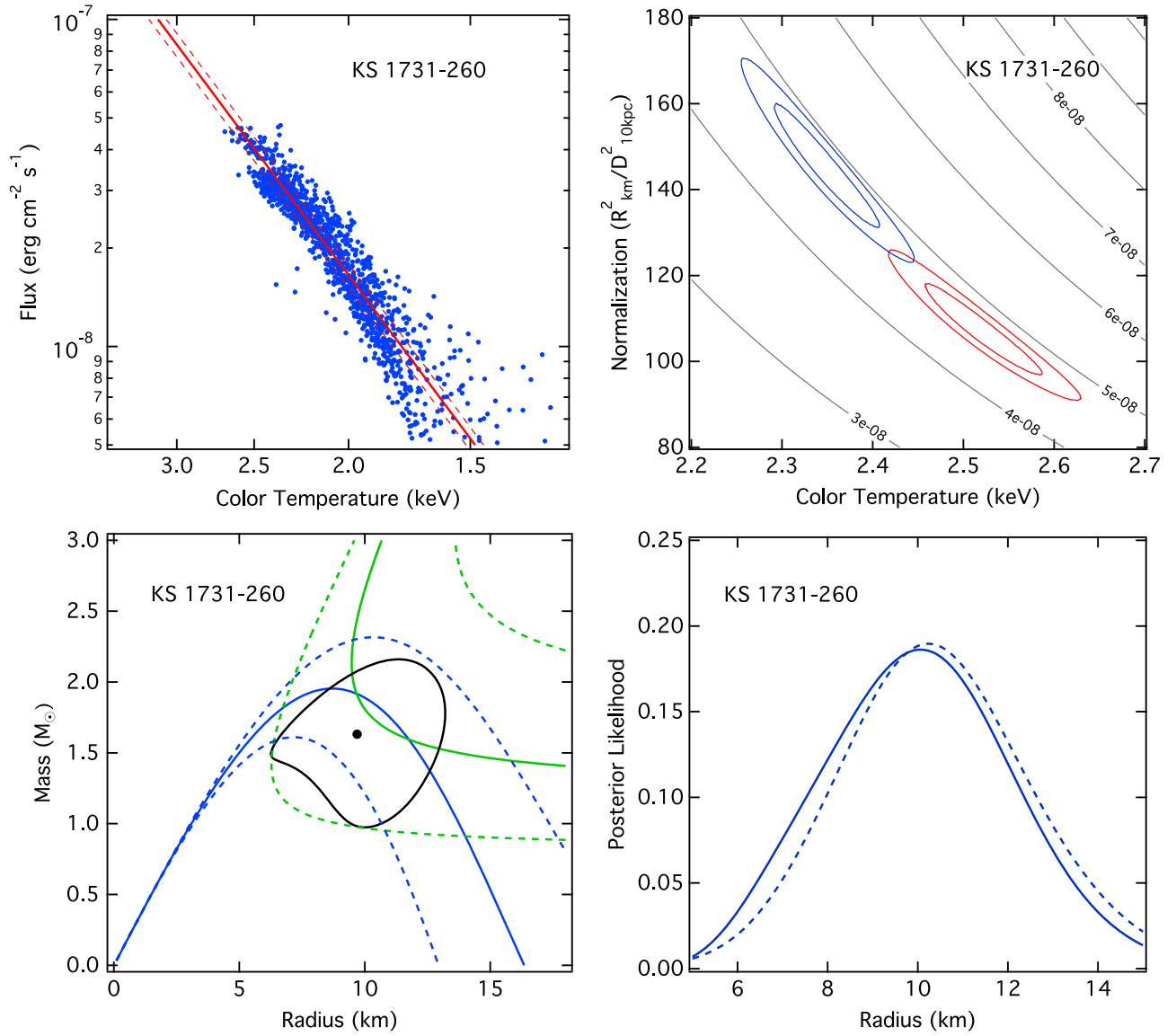
Figure 6. Same as in Figure 3 but for KS 1731−260.

and *Chandra* observations (see Appendix A.2). Finally, the lower panels of Figure 8 show the 68% confidence contour in mass and radius (left) as well as the posterior likelihood marginalized over mass (right).

As with the other sources, these Eddington-limited bursts were selected using the robust photospheric radius expansion (PRE) criteria outlined in Güver et al. (2012a) and form a much smaller sample than those initially identified as potential PRE events by Galloway et al. (2008a). The earlier selection criteria of Galloway et al. (2008a) admitted a large number of non-PRE bursts into the sample, because they were based primarily on the non-monotonic evolution of the inferred apparent radii after the peak of each burst. As discussed in Güver et al. (2012a), careful scrutiny of these bursts clearly demonstrates that the inferred touchdown fluxes (had they been PRE events) are much smaller than the peak fluxes seen in the brightest (true) PRE bursts, in a way that cannot be accounted for by the change in the general relativistic redshift.[8] In addition, the inferred photospheric radii during these misidentified PRE events are comparable to the asymptotic radii of the same bursts. For these reasons, they are not PRE events and do not pass the criteria of Güver et al. (2012a).

3.1.7. Comparison with Previous Work

There are some differences in the mass–radius contours presented here compared to our earlier studies of the same sources. The primary reasons for these differences were discussed at the end of Section 3.1 and include applying appropriate deadtime corrections to the observed count rates, incorporating the measured intrinsic scatter in the measurements (beyond the statistical uncertainties), applying spin and temperature corrections to the apparent angular sizes and touchdown fluxes, and using a Bayesian method to infer

---

[8] This is the same argument used in Galloway et al. (2008b) to reject bursts from high inclination sources.
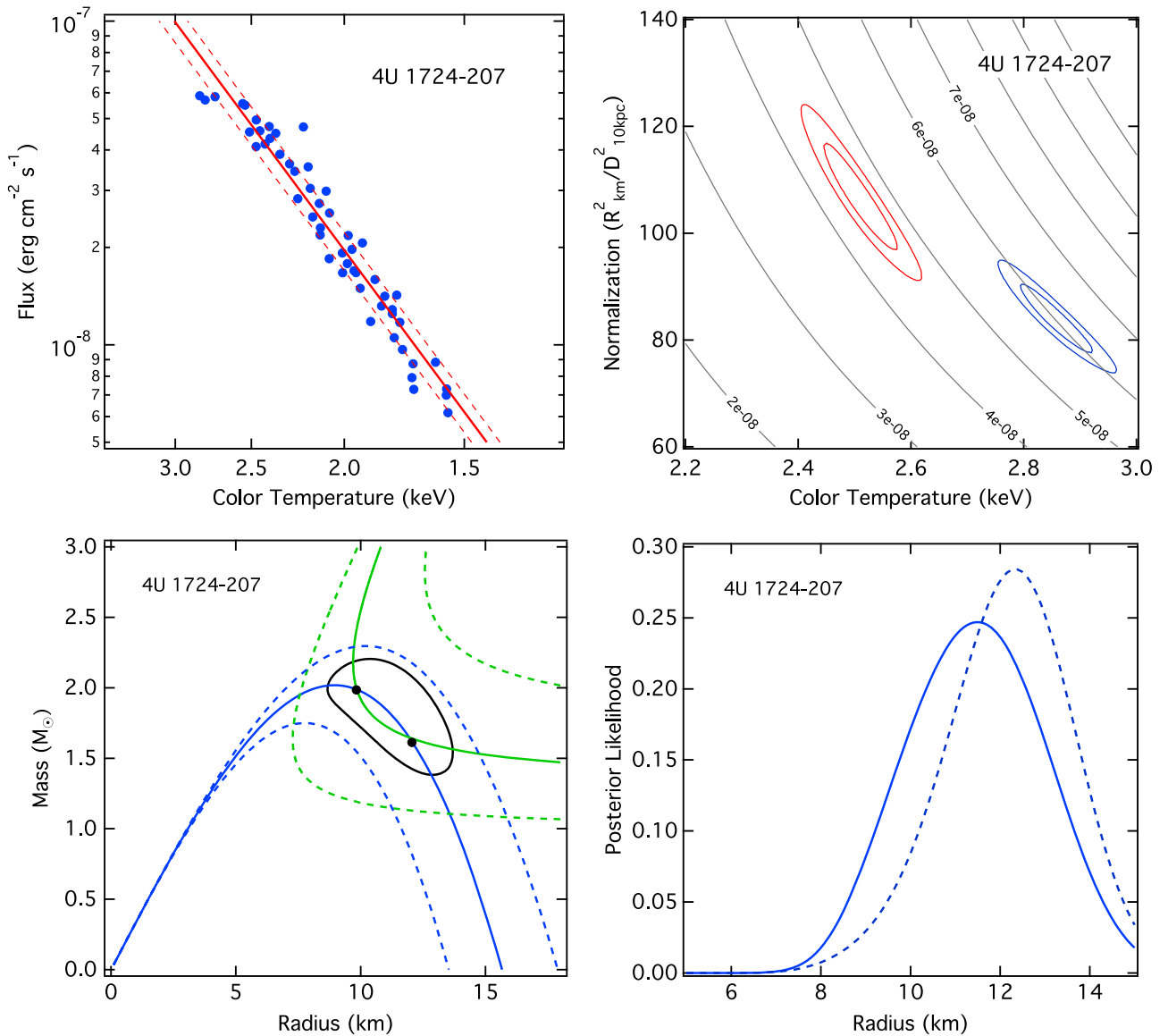
Figure 7. Same as in Figure 3 but for 4U 1724−207.

the masses and radii from the observables that does not suffer from the biases of the earlier frequentist approach. All of these improvements in the analysis methods lead to most likely values for the radii that are $\lesssim 1$ km larger than before (compare with Özel et al. 2010, 2012a; Güver & Özel 2013) but with 68% contours that encompass the most likely radii of the earlier studies.

Our analysis and results are different from those of Steiner et al. (2010, 2013), especially on the upper range of likely values of radii. Steiner et al. (2010) used the measurements reported in Özel et al. (2009) and Güver et al. (2010a, 2010b) but explored a number of different possibilities, including varying the location of the photosphere at the point we identify as the touchdown in a PRE burst. Their analysis favored the assumption that the photospheric radius at that point is much larger than the neutron star radius such that the general relativistic redshift is negligible. They followed this approach because they argued that the two spectroscopic measurements from each source are otherwise inconsistent with each other. In Özel & Psaltis (2015), we demonstrated that this potential inconsistency is alleviated when the true systematic scatter in the measurements is taken into account. Moreover, in Figure 1 we showed the role that the rotational correction to the angular size and the temperature correction to the Eddington flux play in determining the consistency of observables. When these corrections are not taken into account, two highly accurate measurements of these quantities will appear to be inconsistent with each other and will not lead to a solution for the neutron star mass and radius.

As the lower left panels of Figures 3–8 show, taking these effects into account makes the two spectroscopic observables in all sources consistent with each other at the 68% level even when only the most likely values of the distance and the central value of the color correction factor are considered. This is further illustrated in Figure 9, which compares the prior and posterior likelihoods of the blackbody normalization, the touchdown flux, and the distance for 4U 1820−30; this is the source for which Steiner et al. (2010) made the argument that the solutions were the least consistent. As is evident from this figure, combining the two observables leads to posterior likelihoods that are well within the prior likelihoods, indicating a high level of consistency. We report in Table 5 of the Appendix the posterior likelihoods over each of the three measured quantities for all of the six thermonuclear burst sources used in
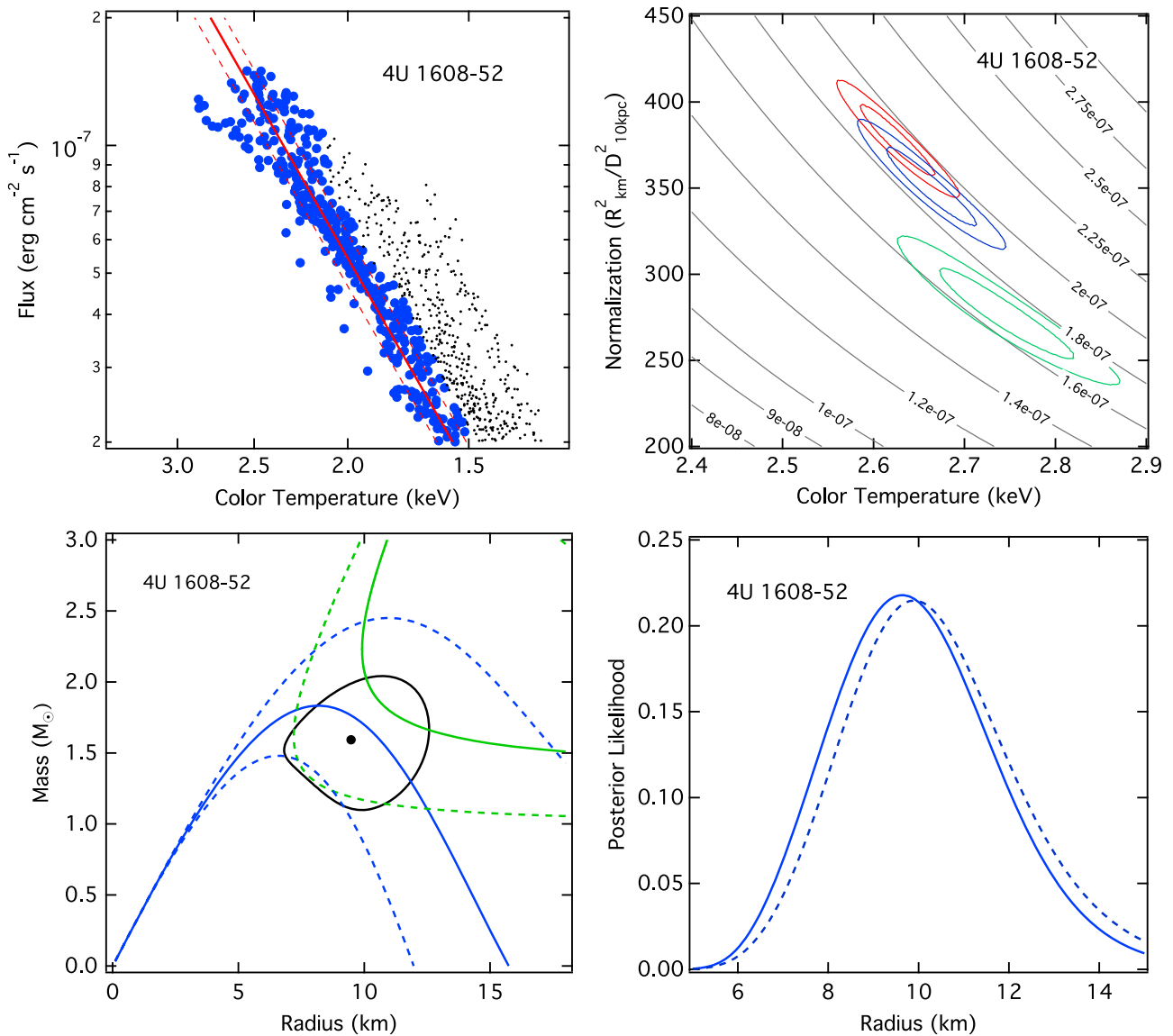
Figure 8. Same as in Figure 3 but for 4U 1608−52. In the upper left panel, the blue points correspond to the main cooling tail and the black points denote the outliers, as discussed in the Appendix.

this study. In all of the cases, the central values of the posterior likelihoods are within the 68% range of the prior likelihoods shown in Table 1, pointing again to a high degree of consistency between the measurements that are used to infer the neutron star radii.

Because the new analysis eliminates the concern over the consistency of solutions, it does not force us into the astrophysically unreasonable assumption of Steiner et al. (2010) that the photosphere that we identified as the touchdown point is much larger than the neutron star radius. This was problematic for two reasons. First, in order for the blackbody normalization to remain small at that point while the photospheric radius is still extremely large, the color correction factor needs to be unphysically large; i.e., larger by factors of three or more than what the atmosphere models predict. Second, within 1–2 time bins, as the photosphere settles onto the neutron star, the color correction factor would need to evolve in such a way that it exactly cancels out the change in the photospheric radius, keeping a constant blackbody normalization. We do not need to make these implicit assumptions in the present study.

Our radii are significantly smaller than those reported by Suleimanov et al. (2011) and Poutanen et al. (2014), who selected bursts and obtained radius measurements using the evolution of the blackbody normalization during the cooling tails of 4U 1724−207 and 4U 1608−52, respectively. In the case of Suleimanov et al. (2011), the selection criteria identified one burst. Unfortunately, as shown in Güver et al. (2012b) and discussed earlier, the spectra from these bursts are inconsistent with the atmosphere models, leading to reduced χ^2 values in the 2−8 range, rendering them unsuitable for radius measurements.

Poutanen et al. (2014) selected bursts from 4U 1608−52 by requiring the bursts to follow the trends expected from the bursting neutron star atmosphere models of Suleimanov et al. (2012) at near-Eddington fluxes. In Özel et al. (2015), we showed that this criterion is not useful for burst selection from *RXTE* data for three reasons. First, the spectral evolution at the end of a PRE episode occurs too rapidly to be resolved with the current data, because over the typical 0.25 s time bin used to extract spectral parameters, the flux evolves by ∼10%. This is exactly the range of fluxes near the Eddington limit that one needs to resolve in order to see the expected evolution of the color correction factor. Second, the scatter in the blackbody normalization due to even a mild change in the
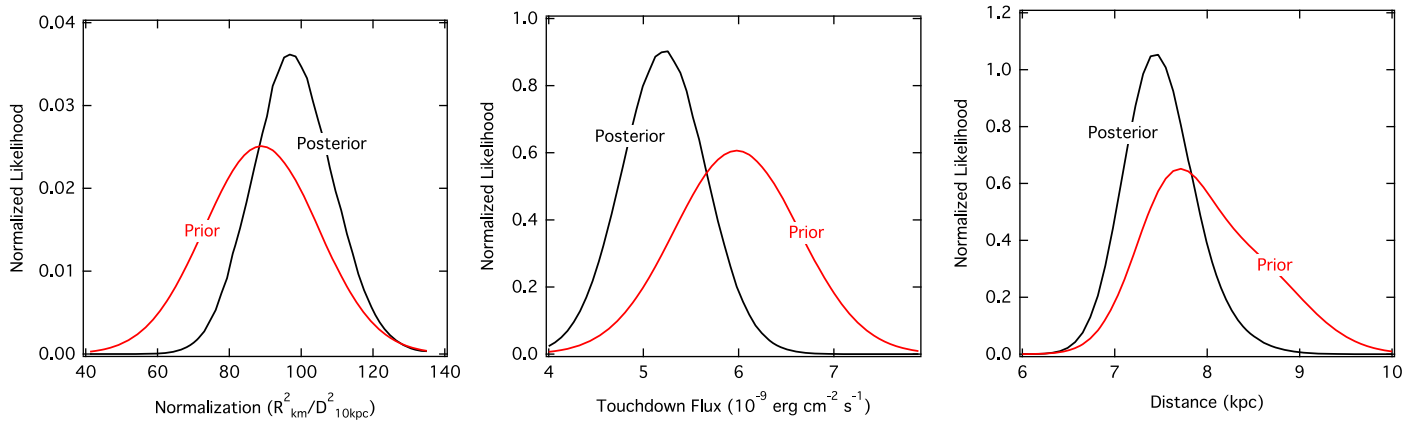
Figure 9. A comparison between the prior and the posterior likelihoods over the blackbody normalization, the touchdown flux, and the distance to 4U 1820−30. When the measured systematic uncertainties in the two spectroscopic measurements, as well as the full prior likelihood over the distance, are taken into account, there is no evidence for inconsistencies between the observables.

emitting area (due to, e.g., uneven burning or an evolving photosphere) masks the theoretical trends. Finally, the correlated measurement uncertainties between the blackbody normalization and temperature further smear any trends. By not taking these data limitations into account, Poutanen et al. (2014) selected a set of bursts that are not actual PRE bursts, contrary to the implicit assumption in their method.

As discussed above, in both the Suleimanov et al. (2011) and Poutanen et al. (2014) studies, applying these theoretically motivated criteria led to the selection of bursts that are inconsistent with the framework of the method: in the former by selecting spectra that are clearly not described by their atmospheric models and in the latter by comparing models of the color correction factor evolution near the Eddington limit to bursts that have not reached it. Kajava et al. (2014) tried to generalize this selection procedure to several more sources (without reporting any additional radius measurements) but also did not consider the limitations of the data. We conclude that with the present data, the application of this procedure motivated by the spectral models leads neither to unbiased data selection, nor to reliable radius measurements.

3.2. Quiescent Low-mass X-Ray Binaries

The second group of sources on which radius measurements have been performed are the accreting neutron stars in low-mass X-ray binaries during their quiescent epochs (qLMXBs). It is thought that, in quiescence, neutron stars reradiate the heat stored in the deep crust during the accretion phases through a light element atmosphere (Brown et al. 1998). This allows interpretation of the observed thermal spectra as surface emission from atmospheres in radiative equilibrium, while allowing for the presence of a weak power-law spectral component at higher energies due to residual accretion. Because of the very short settling time of heavier elements in a neutron-star atmosphere, the photospheres of such neutron stars in quiescence are expected to be composed of hydrogen, unless the companion star is hydrogen poor. In that case, they will be composed of helium.

A number of qLMXBs in globular clusters have been observed with *Chandra* and *XMM-Newton*. Because they are very faint and are located in crowded fields, the high angular resolutions and low backgrounds of these instruments were crucial for obtaining spectroscopic constraints of their apparent angular sizes (e.g., Heinke et al. 2006; Webb & Barret 2007; Guillot et al. 2011).

Guillot et al. (2013) and Guillot & Rutledge (2014) performed a uniform analysis of six sources in this category, which are the neutron stars located in the globular clusters M13, M28, M30, ω Cen, NGC 6397, and NGC 6397. These observations include those summarized in Table 1 of Guillot et al. (2013), as well as the *Chandra* observations of the qLMXB in M30 (ObsID 2679; Lugger et al. 2007) and of the qLMXB in ω Cen (ObsIDs 13726 and 13727), as described in Guillot & Rutledge (2014). These two studies fit the extracted spectra with hydrogen atmosphere models to measure the apparent angular sizes for these neutron stars. They explored the dependence of the results on different hydrogen model atmosphere spectra used. They also allowed for a Gaussian distribution of errors in distances (albeit narrower than the uncertainties we assigned above to bursters in globular clusters) when fitting all of the sources simultaneously.

There are several additional sources of systematic uncertainties that can affect the radius measurements that have been addressed to various degrees: the composition of the atmosphere, the composition and modeling of the interstellar medium that gives rise to the low-energy extinction, and the modeling of the power-law spectral component that is due to residual accretion. The majority of qLMXBs for which optical spectra have been obtained show evidence for Hα emission (Heinke et al. 2014), indicating a hydrogen rich companion. Most of these qLMXBs are in the field and not in globular clusters like the ones we are using here. Assuming that sources in both types of environments have similar companions supports, in general, the use of hydrogen atmospheres when modeling quiescent spectra. The one source among those used here for which there is evidence to the contrary is the qLMXB in NGC 6397. Heinke et al. (2014) obtained only an upper limit on the Hα emission using *HST* observations and because of this, they applied a helium atmosphere model to the *Chandra/XMM-Newton* data sets described above.

Heinke et al. (2014) also explored the effect of assuming different spectral indices in modeling the power-law component. Even though the low counts preclude an accurate measurement of this parameter, the specific value has a small effect on the radius measurement, which can be folded in as a systematic uncertainty. Finally, because of the low temperature of the surface emission from
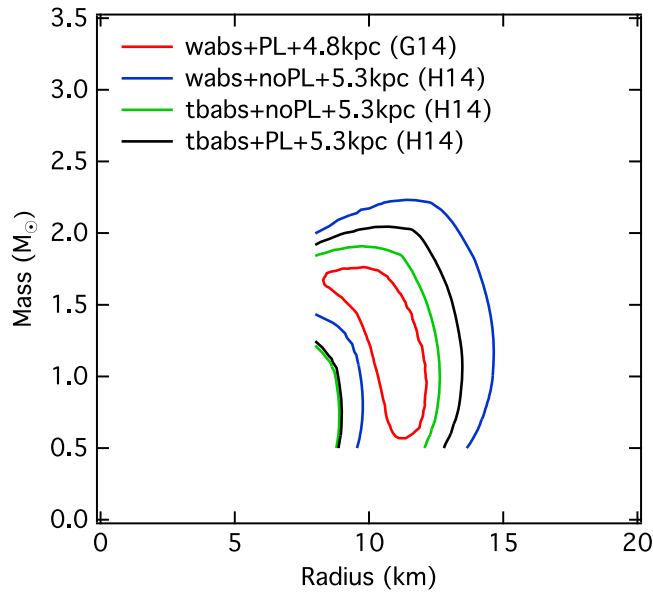
Figure 10. The 68% confidence contours in mass and radius for the quiescent neutron star in ω Cen, inferred by Heinke et al. (2014; H14) and by Guillot & Rutledge (2014); G14) using different assumptions regarding the interstellar extinction (wabs: Morrison & McCammon 1983; tbabs: Wilms et al. 2000), the presence of a power-law spectral component, and for different distances to the globular cluster (4.8 kpc vs. 5.3 kpc).

qLMXBs, the spectral modeling is affected significantly by the assumed model of the interstellar medium to account for the low-energy extinction. Heinke et al. (2014) explored different models for the interstellar extinction in their analysis of the qLMXBs in ω Cen and NGC 6397 and found statistically consistent results, with small differences in the central values but larger differences in the uncertainties. In the left panel of Figure 10, we show the effect of different assumptions on the power-law index, the distance, and the interstellar extinction model on the inference of the mass and radius of the neutron star in ωCen. In particular, one of the larger effects arises from the use of the two common interstellar extinction models they consider (the earlier Morrison & McCammon 1983 model with solar abundances, referred to as wabs in the spectral fitting software XSPEC, and the more recent Wilms et al. 2000 model, with ISM abundances from the same paper, referred to as tbabs with *wilms* in XSPEC). The wabs model (employed by Guillot et al. 2013) leads to somewhat larger radii for the same distance.

In the present study, we repeat the analysis of Guillot et al. (2013) individually for all the sources in M13, M28, NGC 6304, NGC 6397, M30, and ωCen. (Note that for the last two sources, the observations were reported in Guillot & Rutledge 2014). In all of the spectral fits, we allow for a power-law component with a fixed photon index $\Gamma = 1$ but a free normalization. We use the Wilms et al. (2000) ISM abundances in all of the analyses for a uniform treatment of all qLMXBs. We leave the hydrogen column density as a free parameter in the fits and when calculating the posterior likelihoods over mass and radius. We use a hydrogen atmosphere model for all of the sources except the one in NGC 6397, for which we use a helium atmosphere model (see also Heinke et al. 2014). The best-fit spectral parameters for each source are shown in Table 2. We also fold in distance uncertainties using a Gaussian likelihood for the distance to each source with a mean and standard deviation given in Table 2.

We show the resulting posterior likelihoods over the mass and radius for all of the qLMXBs in the right panel of Figure 11 and compare them to the combined constraints from the X-ray bursters discussed earlier. There is a high level of agreement between all of these measurements. Note that the larger widths of the 68% confidence contours of each source compared to those presented in Guillot et al. (2013, their Figures 3–7) are due to the fact that in the present work, we leave the hydrogen column density as a free parameter.[9]

4. THE CONSTRAINTS ON THE NEUTRON STAR RADIUS

Having obtained posterior likelihoods over the mass and radius for a number of neutron stars, we can follow one of the inversion techniques developed earlier to infer the equation of state of neutron star matter. We defer this analysis to the following section and first carry out a simple exercise to illustrate how tight constraints on the equation of state can be obtained when a large number of measurements with relatively large uncertainties is used.

For this purpose, we consider a mono-parametric equation of state in which all neutron stars have the same radius independent of mass. (Note that this is in the same spirit as the CstR$_{NS}$ model of Guillot et al. 2013. It is indeed a meaningful assumption for nearly all nucleonic equations of state, which predict approximately constant radii for the astrophysically relevant mass range.) We also assume that all the neutron stars in our sample are drawn from the observationally inferred Gaussian distribution of masses (see Özel

---

[9] While the simultaneous "Constant Rns" fits of Guillot et al. (2013) were performed by leaving the column density N_H as a free parameter, Figures 3–7 in that study display results from fits performed with fixed N_H. Furthermore, note that the present study also includes additional X-ray data for ω Cen, which refined the M–R contours.

Table 2
Properties of Quiescent LMXBs

Source	N_H [a] $(10^{22}$ cm$^{-2})$	kT_{eff} (eV)	P.L. Norm.[b] $(10^{-7}$ keV^{-1} s^{-1} cm$^{-2})$	Distance[c] (kpc)	Radius[d] (km)
M13	$0.02^{+0.04}_{-0.02}$p	81^{+27}_{-12}	$4.2^{+3.6}_{-3.1}$p	7.1 ± 0.4 (1)	10.9 ± 2.3
M28	$0.30^{+0.03}_{-0.03}$	128^{+35}_{-13}	$8.3^{+4.9}_{-4.7}$p	5.5 ± 0.3 (2)	8.5 ± 1.3
M30	$0.02^{+0.03}_{-0.02}$p	96^{+30}_{-13}	$9.3^{+5.4}_{-5.3}$p	9.0 ± 0.5 (3), (4)	11.6 ± 2.1
ωCen	$0.15^{+0.04}_{-0.04}$	80^{+24}_{-10}	$0.8^{+1.3}_{-0.7}$p	4.59 ± 0.08 (5), (6)	9.4 ± 1.8
NGC 6304	$0.49^{+0.15}_{-0.13}$	100^{+33}_{-17}	$2.4^{+2.7}_{-1.9}$p	6.22 ± 0.26 (7)	10.7 ± 3.1
NGC 6397	$0.14^{+0.02}_{-0.02}$	66^{+17}_{-7}	$3.3^{+1.8}_{-1.8}$	2.51 ± 0.07 (8)	9.2 ± 1.8

Notes.
[a] NGC6397 was fitted with a Helium atmosphere model (nsx in XSPEC).
[b] p indicates that the posterior distribution did not converge to zero probability within the hard limit of the model.
[c] References: (1) Harris (1996, 2010 revision), (2) Servillat et al. (2012), (3) Carretta et al. (2000), (4) Lugger et al. (2007), (5) Watkins et al. (2013), (6) see also the discussion in Heinke et al. (2014), (7) Guillot et al. (2013) and references therein, (8) Heinke et al. (2014).
[d] The radius and its 68% uncertainty obtained by marginalizing the mass–radius likelihood of each source over the observed mass distribution, as in Figure 12.
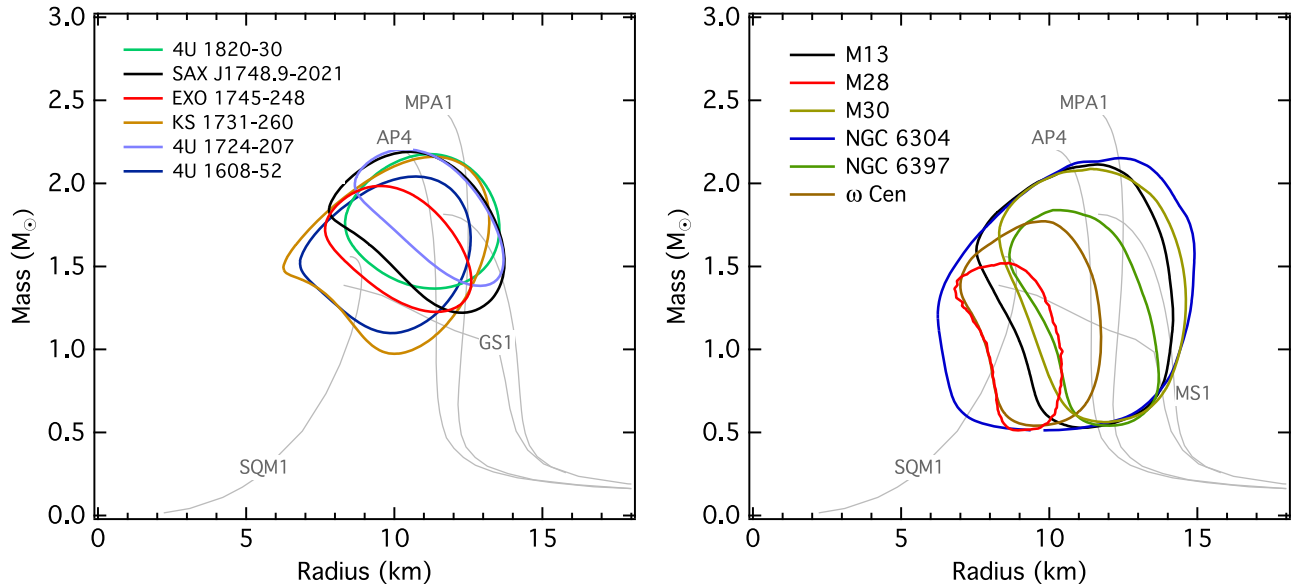

Figure 11. The combined constraints at the 68% confidence level over the neutron star mass and radius obtained from (left) all neutron stars with thermonuclear bursts (right) all neutron stars in low-mass X-ray binaries during quiescence.

et al. 2012b). Specifically, we write

$$P(R \mid \text{data}) = C \prod_{i=1}^{N} \int P_i(R, M \mid \text{data}) P_p(M) dM \qquad (11)$$

where C is an appropriate normalization constant, $P_i(R, M \mid \text{data})$ is the two-dimensional posterior likelihood over mass and radius for each of the N sources (as given, e.g., in Equation (9) for the bursters), and $P_p(M)$ is the Gaussian likelihood with a mean of 1.46 $M_\odot$ and a dispersion of 0.21 $M_\odot$ for the mass distribution inferred by Özel et al. (2012b) for the descendants of these systems.

The left panel of Figure 12 shows the individual terms of the product in the equation above; i.e., the posterior likelihoods over radius for each of the 12 sources. They are all well approximated by Gaussian distributions that peak between 9 and 12 km and typical uncertainties of ~2 km. The right panel of Figure 12 shows the posterior likelihood over the single radius in this mono-parametric equation of state, which is peaked at a radius of 10.3 km with an uncertainty of 0.5 km. As expected, given that all radii are statistically consistent with each other, combining the data of the 12 sources led to a reduction in the uncertainty by a factor of $\sqrt{12} \simeq 3.5$. The result is a level of uncertainty that is comparable to what is required to severely constrain the neutron star equation of state, as we will show in detail in the next section.

5. THE NEUTRON STAR EQUATION OF STATE FROM RADII AND LOW-ENERGY EXPERIMENTS

We now make use of the one-to-one mapping between the neutron star mass–radius relation and the pressure-density relation of cold dense matter to put direct constraints on the neutron-star equation of state. In this procedure, we take the most general approach
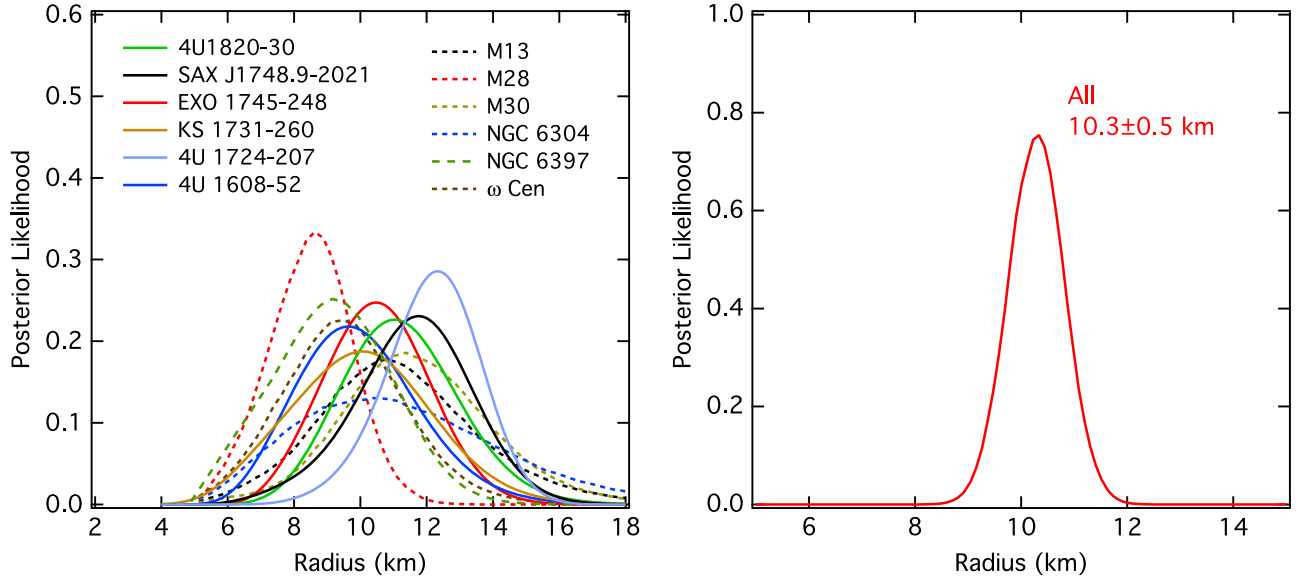
Figure 12. (Left) The posterior likelihood over the radius obtained by marginalizing the two dimensional likelihoods over the neutron star mass, with a prior equal to the observationally inferred distribution of recycled pulsar masses, for all 12 sources in our sample. The peak probabilities are highly clustered in the 9–12 km range. (Right) The combined posterior likelihood assuming that all sources in our sample have the same radius and masses drawn from the observationally inferred distribution of recycled pulsar masses. We use this inference only as an illustration of the fact that using radius measurements for the 12 sources leads to a highly accurate constraint on the neutron-star equation of state.

and do not assume that neutron stars have a constant radius or make assumptions about their masses based on the observationally determined mass distribution.

The structure equations for relativistic stars provide, for each equation of state, a unique mass–radius curve, with no adjustable parameters. Because of this, a large number of radius measurements across a range of neutron star masses allow us to invert the measurements formally and obtain the unique equation of state that gave rise to the measured mass–radius pairs (Lindblom 1992). Moreover, more recent parametric forms of the equation of state that do not rely on particular nuclear physics models (e.g., Read et al. 2009; Özel & Psaltis 2009; Steiner et al. 2010; Lattimer & Steiner 2014b) allow us to put this inversion into practice even without sampling the entire mass–radius curve. This is because the radii of astrophysically relevant neutron stars turn out to be sensitive to the equation of state in a fairly narrow range of densities between 1.8 and 7.4 times the nuclear saturation density (ρ_{ns}) and this in turn enables a discretization of the equation of state over this narrow range of densities using only three sampling points that are connected by piecewise polytropes (Read et al. 2009; Özel & Psaltis 2009). Using the SLy equation of state (Douchin & Haensel 2001) up to a density of $\rho_0 = 10^{14}$ g cm^{-3} and taking the fiducial densities at 1.85 ρ_{ns}, 3.7 ρ_{ns}, and 7.4 ρ_{ns}, which we denote as ρ_1, ρ_2, and ρ_3, respectively, these studies have shown that the discretized equations of state generate mass–radius relations that faithfully reproduce the mass–radius relations of the continuous $P(\rho)$ functions for a large number of proposed equations of state. Of these three pressures, the pressure at 1.85 ρ_{ns} sets the overall radii of neutron stars, the pressure at 3.7 ρ_{ns} determines the slope of the predicted M–R relation, and the pressure at 7.4 ρ_{ns} sets the maximum mass.

In Özel et al. (2010), we used the framework devised in Özel & Psaltis (2009) to convert the mass–radius measurements of three sources to posterior likelihoods over the pressures at these three fiducial densities. In order to incorporate the mass–radius measurements of the twelve sources presented in Section 3, here we will follow the Bayesian approach outlined below. (See Steiner et al. 2010 for a similar Bayesian inference approach.)

To calculate the posterior likelihood over the pressures $P_1(\rho_1)$, $P_2(\rho_2)$, and $P_3(\rho_3)$ using the likelihoods $P_i(M, R)$ for the 12 sources, we write

$$P(P_1, P_2, P_3 \,|\text{data}) = CP(\text{data} \,|\, P_1, P_2, P_3)P_p(P1)P_p(P_2)P_p(P_3), \qquad (12)$$

where $P_p(P1)$, $P_p(P_2)$, and $P_p(P_3)$ are the priors over the three pressures and

$$P(\text{data} \,|\, P_1, P_2, P_3) = \prod_{i=1}^{N} P_i(M_i, R_i \,|\, P_1, P_2, P_3). \qquad (13)$$

To obtain (M_i, R_i) from the pressures P_1, P_2, P_3, we also need to specify, and marginalize over, the central density of the star ρ_c, i.e.,

$$P_i(M_i, R_i \,|\, P_1, P_2, P_3) = C_1 \int_0^\infty P_i(M_i, R_i \,|\, P_1, P_2, P_3, \rho_c)P_p(\rho_c)d\rho_c. \qquad (14)$$

16

Because there is a one-to-one correspondence between the central density ρ_c and mass, we can write the integral over the mass instead as

$$P_i(M_i, R_i \mid P_1, P_2, P_3) = C_2 \int_{M_{\min}}^{M_{\max}} P_i(M, R(M) \mid P_1, P_2, P_3) P_p(M) dM, \qquad (15)$$

where we take $M_{\min}$ to be $0.1\,M_\odot$ and $M_{\max}$ to be the maximum mass for the equation of state specified by that P_1, P_2, P_3 triplet. Here, $P_p(M)$ is the prior likelihood over the mass of each neutron star, which we take to be constant.

We use a variety of physical and observational constraints to define the priors on P_1, P_2, and P_3.

   (i) We require that the equation of state be microscopically stable, i.e., $P_3 \geqslant P_2 \geqslant P_1$, and that P_1 be greater than or equal to the pressure of matter at $\rho_0 = 10^{14}\,\mathrm{g\,cm^{-3}}$ that is specified by the SLy equation of state (see Özel & Psaltis 2009).
  (ii) We impose the physically plausible condition of causality that

$$c_s^2 = \frac{\partial P}{\partial \epsilon} \leqslant c^2 \qquad (16)$$

when evaluated at all three fiducial densities; here, c_s is the sound speed and ϵ is the energy density.
 (iii) We require that the maximum stable mass for each equation of state corresponding to a P_1, P_2, P_3 triplet exceeds $1.97 M_\odot$, consistent with the heaviest neutron stars observed to date. Specifically, this corresponds to the central value of the measurement by Demorest et al. (2010) and is within the 1σ lower limit of the measurement by Antoniadis et al. (2013).
 (iv) We impose a lower limit on $P_1 = 7.56\,\mathrm{MeV\,fm^{-3}}$ such that the equation of state is consistent with laboratory experiments and low density calculations, as we will describe in detail below. This value is quantitatively consistent with the APR equation of state for pure neutron matter (Akmal et al. 1998).
  (v) Finally, in order to explore the dependence of our results on the prior distributions, we consider two sets: one that is flat in $\log P_1$, $\log P_2$, and $\log P_3$, and one that is flat in P_1, P_2, and P_3.

The first two constraints are required on microphysical grounds (but see Bludman & Ruderman 1968 and Ellis et al. 2007 for caveats on the causality argument). In the next two constraints, we fold in information about the equation of state inferred from other astrophysical observations or nuclear experiments. This ensures that the equation of state derived from neutron star radii is consistent with these other results. In addition, combining these several different avenues of information allows us to achieve the highest precision in the resulting constraints.

Our understanding of the equation of state in the vicinity of the nuclear saturation density is firmly founded on nucleon–nucleon scattering experiments below 350 MeV and on the properties of light nuclei. An approach that makes use of these data most directly is based on describing the interactions between particles via static two- and three-body potentials at this density (Akmal et al. 1998). As we noted in Özel et al. (2010), beyond a few times nuclear saturation density, the interaction between particles can no longer be described by static few-body potentials, and at even higher densities, a well-defined expansion in terms of two-, three-, or many-body forces no longer exists. For this reason, the most model-independent constraint that we can impose is on P_1, i.e., at $\rho_1 = 1.85\rho_{\rm ns}$. Following Gandolfi et al. (2012), we consider the expansion of the interaction in terms of two- and three-body potentials and use the contribution of the two-body potential (Argonne AV8) to determine a lower bound to the pressure at $1.85\,\rho_{\rm ns}$. We obtain $P_1 = 7.56\,\mathrm{MeV\,fm^{-3}}$ using AV8, but essentially the same result is found with the AV18 potential.

Using the two nucleon interaction pressure as an absolute lower bound is justified by the fact that the three-body interactions in pure neutron matter are always repulsive (J. Carlson 2015, private communication); including their contributions serves to increase the pressure (see, e.g., Pieper et al. 2001 and Gandolfi et al. 2012, for pure neutron matter; see also Figure 3 of Akmal et al. 1998). The δv relativistic boost correction, which we do not include, also gives a positive contribution to the pressure when calculated with the two body interaction alone. Note though that the contributions of the three body forces and the relativistic boost corrections are not simply additive.

A few words of caution are in order. In symmetric nuclear matter at nuclear matter density, the three nucleon interaction is quite attractive at nuclear matter density, as it must be to achieve sufficient binding energy for light nuclei; the three nucleon interaction turns repulsive only for densities roughly above $1.5\,\rho_{\rm ns}$. Furthermore, the three nucleon interaction including the relativistic boost correction, softens the equation of state of symmetric nuclear matter above nuclear matter density. While the three nucleon interaction as implemented in the APR equation of state is indeed repulsive in pure neutron rich matter, there remain theoretical uncertainties in the interaction itself. One should, in addition, take into account the modification of the effects of the three body interaction when imposing beta equilibrium and hence allowing for a finite proton fraction; as can be seen from Figure 16 of Akmal et al. (1998), the three body interaction again increases the pressure. A further complication is the onset of a neutron pion-condensed phase in neutron rich matter at a density $\sim 0.2\,\mathrm{fm^{-3}}$, which lowers the pressure (as can be seen for pure neutron matter in Figure 5 of Akmal et al. 1998).

In Figure 13, we show the posterior likelihoods over the pressures at the three fiducial densities, as well as the microscopic and experimental bounds on these pressures. We also plot the pressures of a number of proposed equations of state with widely differing assumptions and calculation techniques. Because pressure P_1 has the largest effect on the stellar radius, it is significantly constrained by the radius data from above. The lower limit on P_1 coming from the two-body interaction potential obtained at low densities excludes the gray region labeled 2NI. The most likely value, as well as the entire region within the highest posterior likelihood, are, in fact, lower than the pressure predicted by most equations of state at that density, as shown in the lower panel (see Read et al. 2009 for the acronyms and the references for the various equations of state). We also include in this figure the recent equation of state labeled
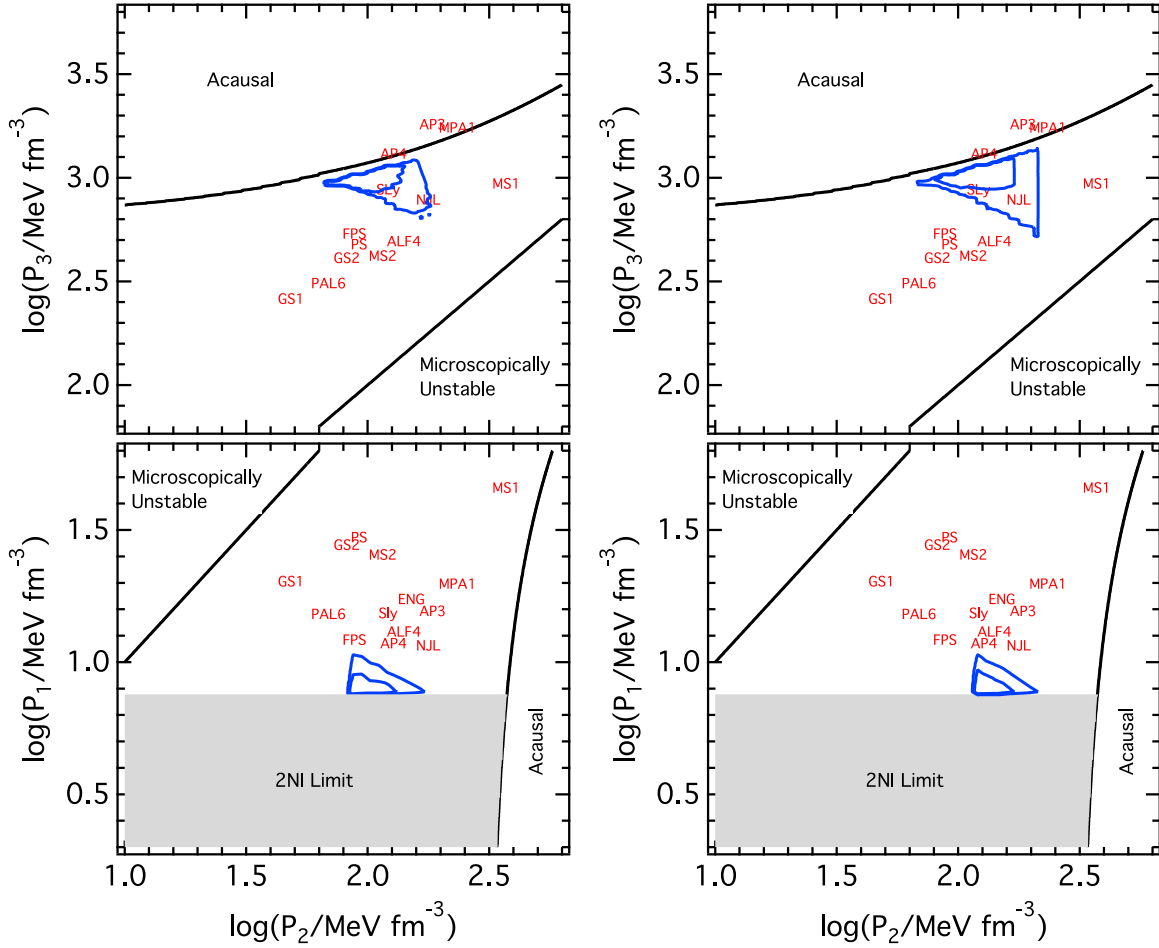
Figure 13. The highest likelihood regions in the pressure of neutron star matter at 1.85 ρ_{ns} (P_1), 3.7 ρ_{ns} (P_2), and 7.4 ρ_{ns} (P_3) obtained by a parametric inversion of all the neutron star radius measurements. To visualize the structure of the three-dimensional posterior likelihood function, the contours outline the regions in which the posterior likelihoods drop down to $e^{-1/2}$ and e^{-1} of the highest value. The allowed regions of the parameter space are consistent with the constraints from calculations based on low-energy scattering experiments, are microscopically stable, and ensure that the equation of state remains causal. The left panel shows the result for flat priors in the logarithms of P_1, P_2, and P_3, while the right panel shows the result for flat priors in P_1, P_2, and P_3 within the physically allowed ranges of these parameters.

NJL (Kojo et al. 2015), based on a smooth interpolation in pressure versus baryon chemical potential of a nucleonic equation of state (APR) at densities below $\sim\rho_{ns}$ with a quark matter equation of state at densities above $\sim$5–7 ρ_{ns}.

The combination of P_2 and P_3, on the other hand, is constrained by the maximum mass requirement: a lower value of P_2 pushes P_3 to be as high as possible within the causality limit, whereas for moderate to high values of P_2, which already lead to M–R relations that allow high mass stars and are consistent with the radius measurements, the allowed range of P_3 extends to lower values. The combination of P_2 and P_3 excludes to high confidence the stiff equations of state such as MPA1 and MS1, which produce radii that are too large (see also their inconsistency with P_1 in the lower panel). This combination also excludes equations of state with condensates, such as GS1, with pressures that are too low to be consistent with the maximum mass requirement.

Figure 13 shows that the combination of the radius measurements with the low density experimental data and the requirement of a $\sim$2 $M_\odot$ maximum mass pins down the parameters of the equation of state extremely well across a wide range of supranuclear densities and points to a preferred equation of state that is somewhat softer than the nuclear equation of state AP4 (a version of the APR equation of state). To see this on the mass–radius plane, we also show in Figure 14 the mass–radius relation corresponding to the most likely triplet of pressures as well as the range of mass–radius relations for the region of the (P_1, P_2, P_3) parameter space with the highest likelihood. We limit the range of masses in this figure to $\leqslant$2.2 $M_\odot$ because of the absence of any data to constrain the relation at higher masses. As expected from the above discussion, the preferred mass–radius relation lies to the left of most model predictions and is closest to AP4, especially at low masses, where the main uncertainty in AP4 is in the strength of the three-nucleon interactions. It also rises along a nearly constant radius in order to reach the $\sim$2 $M_\odot$ limit. Depending on the choice of the prior (i.e., flat prior on P or log P), the predicted radius for a 1.5 $M_\odot$ neutron star is between 10.1 and 11.1 km.

Because of the relatively narrow range of the statistically acceptable values of the three pressures, the effect of changing the prior distributions is only marginal. It leads to a small shift in the most likely values of the pressures and a change in the predicted radii that is $\sim$0.4 km. This is similar in magnitude to the result obtained by Steiner et al. (2013), even when they considered extreme scenarios (see their Figure 3).

When compared to the earlier inference of Özel et al. (2010) of the pressures at three fiducial densities, the current measurements point to much more constrained values of P_1 and to larger values of P_2 and P_3 by $\sim$0.3 dex. There are three reasons for this change.
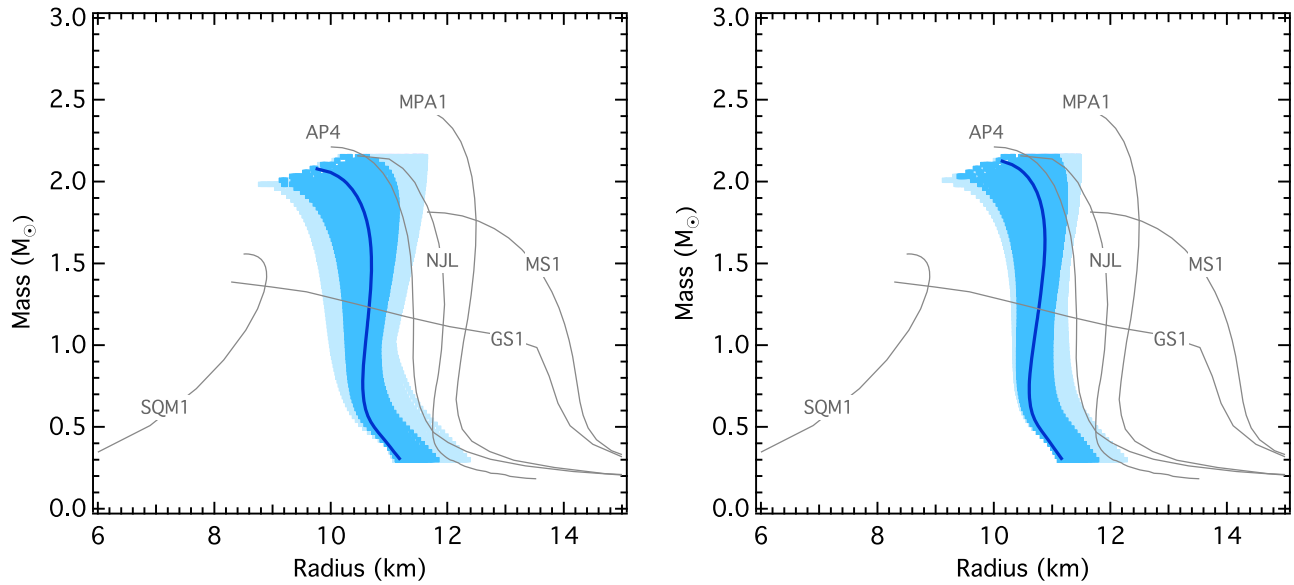
Figure 14. The mass–radius relation (solid blue curve) corresponding to the most likely triplet of pressures that agrees with all of the neutron star radius and low energy nucleon–nucleon scattering data and allows for a $M > 1.97 M_\odot$ neutron star mass. The ranges of mass–radius relations corresponding to the regions of the (P_1, P_2, P_3) parameter space in which the likelihood is within $e^{-1/2}$ and e^{-1} of its highest value are shown in dark and light blue bands, respectively. The left panel shows the result for flat priors in the logarithms of P_1, P_2, and P_3, while the right panel shows the result for flat priors in P_1, P_2, and P_3 within the physically allowed ranges of these parameters.

First, in the present study, we include the radius measurements from qLMXBs. Second, as discussed in Section 3.1.7, the improved analysis methods lead to radii from bursters that are larger by $\lesssim 1$ km. Third, we incorporate the fact that, since that study, two $\sim 2 M_\odot$ neutron stars have been discovered. This effectively places a lower limit on the slope of the mass–radius relation, controlled by P_2, and its turnover point, controlled by P_3 (see Özel & Psaltis 2009; Lattimer & Prakash 2010).

Guillot et al. (2013) used the qLMXBs and a constant radius model to infer typical neutron star radii of 9.4 ± 1.2 km, which also indicate low values of P_1. Even though this inference is not statistically inconsistent with our measurement, the small differences can be understood in terms of the different distances and absorption model used here, compared to those of Guillot et al. (2013). We also incorporate the radius measurements from thermonuclear bursts as well as the mass limits from the heaviest known neutron stars.

Our results point to smaller neutron star radii by ~ 1 km and to lower pressures than the analyses of Steiner et al. (2010, 2013) and Lattimer & Steiner (2014a). As explained in Section 3.1.7, in their analysis of the burst data, these authors obtained larger radii because of their assumption regarding the location of the photosphere at touchdown. In their analysis of the data from several qLMXBs, Lattimer & Steiner (2014a) also obtained larger radii by using a range of estimated values of N_H to alter the M–R contours from Guillot et al. (2013), instead of reanalyzing these data. Because of the strong correlation between N_H and the apparent radius at infinity, this method underestimates the width of M–R contours reported in that study. Finally, they assumed different distances to some of the globular clusters, as well as helium atmospheres for any qLMXB other than ωCen, all of which push the inferred radii to larger values.

6. CONCLUSIONS

We performed a comprehensive study of spectroscopic radius measurements of neutron stars using thermonuclear bursters and quiescent low-mass X-ray binaries. We included a number of corrections to the mass–radius inference that have recently been calculated, incorporated systematic uncertainties in the measurements, and employed Bayesian statistical tools to map the observed quantities to neutron star masses and radii and the latter to the neutron star equation of state.

Using a total of 12 sources allows us to place strong and quantitative constraints on the properties of the equation of state between ≈ 2–8 times the nuclear saturation density, even though the individual measurements themselves do not have the precision to lead to tight constraints. We find that around $M = 1.5 M_\odot$, the preferred equation of state predicts a radius of 10.1–11.1 km. When interpreting the constraints on the pressure at $1.85 \, \rho_{ns}$ in the context of an expansion in terms of few-body potentials (see, e.g., Akmal et al. 1998; Pieper et al. 2001; Hebeler et al. 2010; Gandolfi et al. 2012), our results suggest a relatively weak contribution of the three-body interaction potential. In the framework of quark matter equations of state, the inferred lower pressure at $1.85 \, \rho_{ns}$ is consistent with an increased effective pairing interaction in the interpolated equation of state (the NJL parameter H) at densities $\gtrsim 2 \rho_{ns}$. While one can see this effect in model dependent calculations (Kojo et al. 2015), such a lower pressure is physically reasonable, independent of any particular model, since quark matter at lower densities, en route with decreasing density to the strong three quark correlations that eventually become well defined nucleons, is expected to have greater pairing correlations than at higher density. Accounting for all sources of the inferred pressure decrease remains a theoretical challenge.

Even though we have taken into account a large number of systematic effects in both the observations and in the theoretical framework in the present work, our conclusion still relies on the validity of the astrophysical interpretation of two phenomena, namely, Eddington-limited thermonuclear bursts and the emission from neutron stars in quiescence. We rely on the assumptions that the entire neutron star surface is visible during the cooling tails of bursts and during quiescence, that the Eddington limit is reached in

PRE bursts, and that the surface compositions in quiescence are dominated by hydrogen due to gravitational settling, unless there is evidence to the contrary. The fact that the two sets of measurements are in agreement with each other strongly argues against an overall systematic bias. Nevertheless, radius measurements obtained by non-spectroscopic techniques with potential biases that are different than spectroscopic ones will be necessary to confirm the results of our study. Pulse profile modeling with observations with NICER and LOFT will offer such an opportunity in the near future.

APPENDIX

A.1. Distance to 4U 1608−52

In Güver et al. (2010a), we measured the distance to the neutron star in the X-ray binary 4U 1608−52 using a technique that relies on comparing the hydrogen column density measurement to the equivalent infrared extinction obtained from red clump stars along the line of sight. In order to obtain the hydrogen column density N_H in a way that does not depend on the assumed continuum model, we made use of X-ray grating data and measured the absorption edges of individual elements in the spectra caused by the attenuation in the ISM. At that time, the only suitable X-ray data set was a short *XMM-Newton* RGS data obtained in 2003.

On 2010 March 1, *RXTE*-ASM count rate of 4U 1608−52 started a systematic increase, as expected from an outburst. Based on this, we triggered a *Chandra* DDT observation, which was performed on March 15. We obtained high resolution MEG spectra with these observations, with a total number of counts that was comparable to the archival XMM-Newton observation. Using these grating spectra, we determined the column density of Mg and Ne elements along the line of sight, which we discuss below. We also present the new resulting source distance obtained with these new data.

Chandra observed 4U 1608−52 on 2010 March 15 with a net exposure time of 23.08 ks using ACIS HETG in CC mode (OBSID:12127). The calibration and the extraction of the 1st order grating spectra was performed using TGCAT[10] scripts (Huenemoerder et al. 2011) with CIAO v4.3 and CALDB v.4.1.5.

Following the analysis detailed in Güver et al. (2010a), we fit the Mg and Ne edges using the MEG +/−1st order data using *Sherpa* software (Freeman et al. 2001; Doe et al. 2007). Due to its low number of counts, we did not use the HEG data in this analysis. We binned the spectra to have at least 50 counts in each spectral channel. We show the data and the best-fit continuum model in Figure 15 and the best fit values for both edges in Table 3. The total hydrogen column density inferred from the *Chandra* observation is $(1.09 \pm 0.16) \times 10^{22}$ cm^{-2} assuming ISM abundances (Wilms et al. 2000), which is in excellent agreement with the value $(1.08 \pm 0.16) \times 10^{22}$ cm^{-2} that was found by Güver et al. (2010a). Combining these two measurements, we found a hydrogen column density of $(1.085 \pm 0.113) \times 10^{22}$ cm^{-2} to 4U 1608−52.

The good agreement between measurements separated by seven years indicates that the column density is dominated by absorption in the interstellar medium as opposed to the absorption that is intrinsic to the binary, which is variable (see Miller et al. 2009). Therefore, the distance measurement to 4U 1608−52 using this technique is not significantly affected from possible intrinsic absorption in the system.

To convert the equivalent hydrogen column density to an optical extinction, we used the most recent results in the relation between these two quantities. Foight et al. (2015) analyzed the archival *Chandra* observations of all the supernova remnants used in the Güver & Özel (2009) study to improve the relation between the optical extinction A_V and the hydrogen column density N_H. Performing a uniform analysis of the data set and taking into account the abundances of the interstellar matter (Wilms et al. 2000), Foight et al. (2015) determined the relation between these parameters as $N_H = (2.87 \pm 0.12) \times 10^{21} A_V$. Note that the higher coefficient found by Foight et al. (2015) is primarily because of using different abundances for the ISM. We used this improved relation to convert the hydrogen column density found from the X-ray spectral analysis to optical extinction, and following the same methods detailed in Güver et al. (2010a), we found that the optical extinction A_V to the X-ray binary is 3.78 ± 0.42 mag, which corresponds to a near-IR extinction of $A_K = 0.42 \pm 0.11$ using the relation of Cardelli et al. (1989). The errors here reflect those arising from the uncertainties in the hydrogen column density as well as those arising from the uncertainties in the conversions.

We compare in Figure 16 the extinction values derived above with the extinction curve derived using the red clump giants in the field of view of 4U 1608−52 (see Güver et al. 2010a). Using this, we show in Figure 17 the derived likelihood over the distance to 4U 1608−52, which indicates a source distance of $D > 3$ kpc and the most likely distance at 4 kpc.

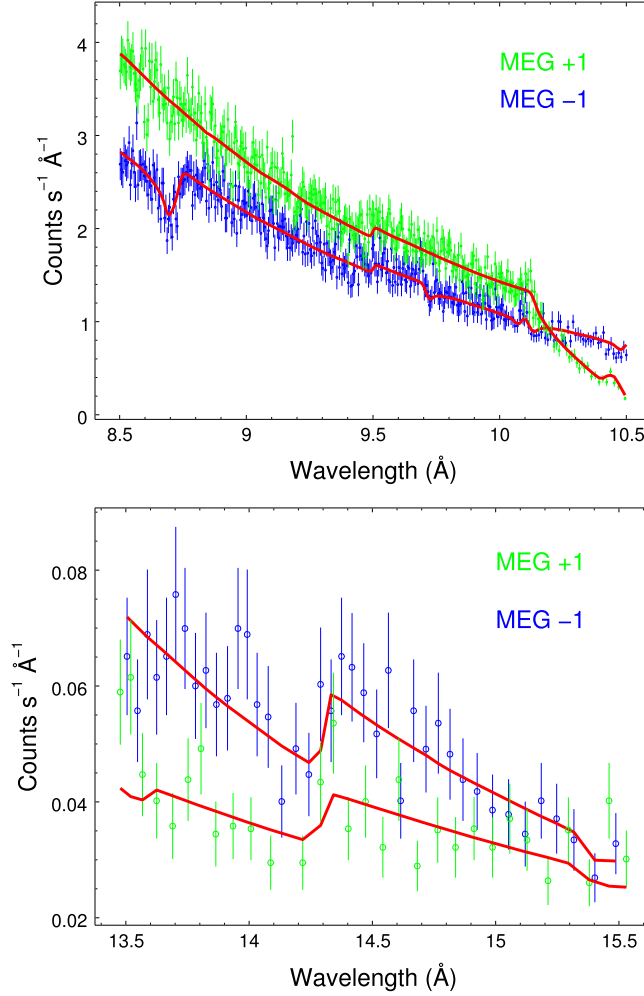[10] http://space.mit.edu/cxc/analysis/tgcat/index.html

Figure 15. *Chandra* medium energy grating data and the best fit model around the Mg edge at $\lambda = 9.5$ Å (top panel) and the Ne edge at $\lambda = 14.3$ Å (bottom panel).

Table 3
Best-fit Values for the Mg and Ne Edges

Edge	Grating	Absorption Coefficient	N $(10^{17}\ \mathrm{cm}^{-2})$	N_{H} $(10^{22}\ \mathrm{cm}^{-2})$	χ^2/dof
Mg	MEG−1	0.067 ± 0.017	3.06 ± 0.75	1.22 ± 0.30	⋯
	MEG+1	0.067 ± 0.015	3.06 ± 0.66	1.22 ± 0.26	⋯
	Combined	0.067 ± 0.011	3.06 ± 0.50	1.22 ± 0.20	0.919
Ne	MEG−1	0.28 ± 0.10	7.95 ± 2.83	0.91 ± 0.33	⋯
	MEG+1	0.26 ± 0.12	7.40 ± 3.41	0.85 ± 0.40	⋯
	Combined	0.27 ± 0.08	7.66 ± 2.27	0.88 ± 0.26	0.844

A.2. The Photospheric Radius Expansion and Cooling Tails of 4U 1608−52 Bursts

RXTE carried out an observation of 4U 1608−52 that was simultaneous with the *Chandra* DDT observation. During the coincident observing period, we detected a very bright X-ray burst ≈2800 s after the *Chandra* observation started, which corresponds to MJD 58070.18852974 (ObsID: 95334-01-03-08).

Following the methods outlined in the previous papers (see, e.g., Güver et al. 2012a, 2012b,) we performed time-resolved X-ray spectroscopy on the *RXTE* PCA data of the burst and measured the 2–10 keV flux, the spectral temperature obtained by fitting the spectrum with a blackbody, and the blackbody normalization (i.e., the apparent angular size). The evolution of the spectral parameters during the burst is shown in Figure 18. With a peak blackbody normalization of ≈6400 $(R^2_{\mathrm{km}}/D^2_{10\,\mathrm{kpc}})$, which is the highest ever reached by this source, the X-ray burst shows clear evidence of a PRE event. Extrapolating from the Galloway et al. (2008a) catalog, we use the ID number 32 for this burst and incorporate it into the touchdown flux and the apparent angular size measurement of 4U 1608−52.

Table 4
Burst IDs Used in the Analysis

Source Name	Burst ID[a] for Touchdown Flux	Burst ID for App. Angular Size
4U 1820−30	1, 2, 3, 4, 5	1, 2, 3, 4, 5
SAX J1748.9−2021	1, 2	1, 2, 15, 16
EXO 1745−248	21, 22	21, 22
KS 1731−260	8, 9	3, 4, 5, 6, 7, 8, 9, 10, 11, 12, 13, 14, 15, 16, 17, 18, 19, 20, 21, 22, 23, 24, 25, 27
4U 1608−52	5, 23, 32	1, 2, 4, 5, 8, 9, 10, 12, 13, 14, 15, 16, 17, 21, 22, 23, 24, 25, 26, 27, 28, 30, 31, 32

Notes.
[a] Burst ID numbers follow the Galloway et al. (2008a) numbering system.
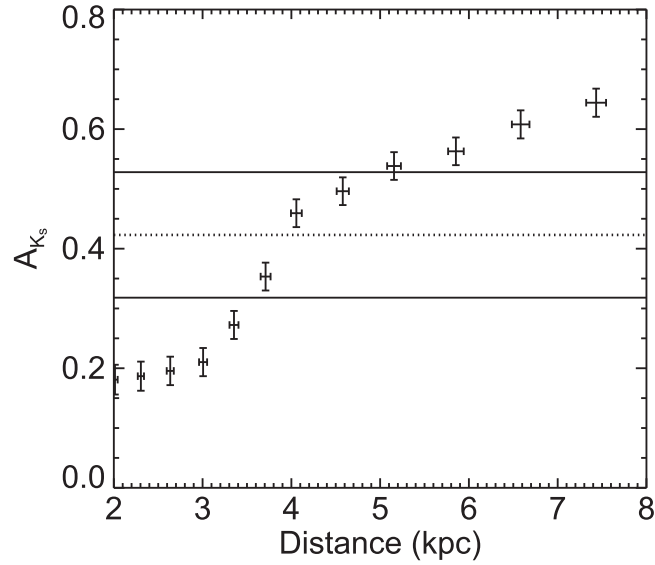
Figure 16. The data points show the evolution of the extinction with distance along the line of sight to 4U 1608−52 as presented by Güver et al. (2010a). The lines show the best-fit value of A_K of the source as derived from high resolution X-ray spectroscopy.
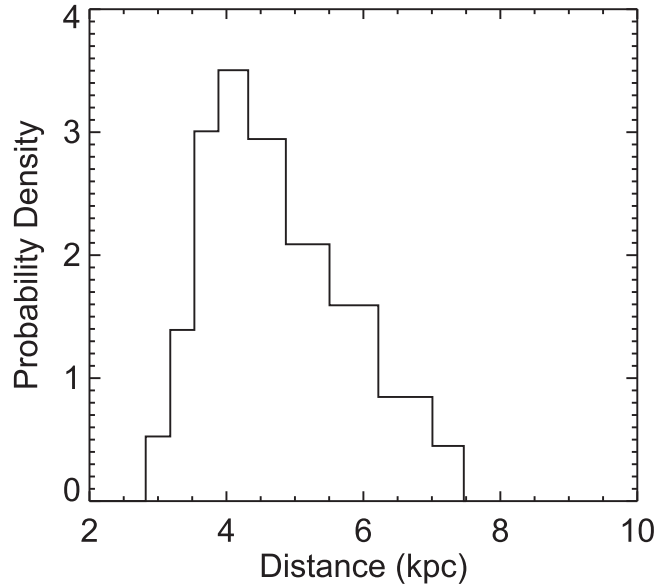

Figure 17. The likelihood over the distance to 4U 1608−52, which indicates that it lies at a distance of $D > 3$ kpc and has the highest likelihood at $D \approx 4$ kpc.
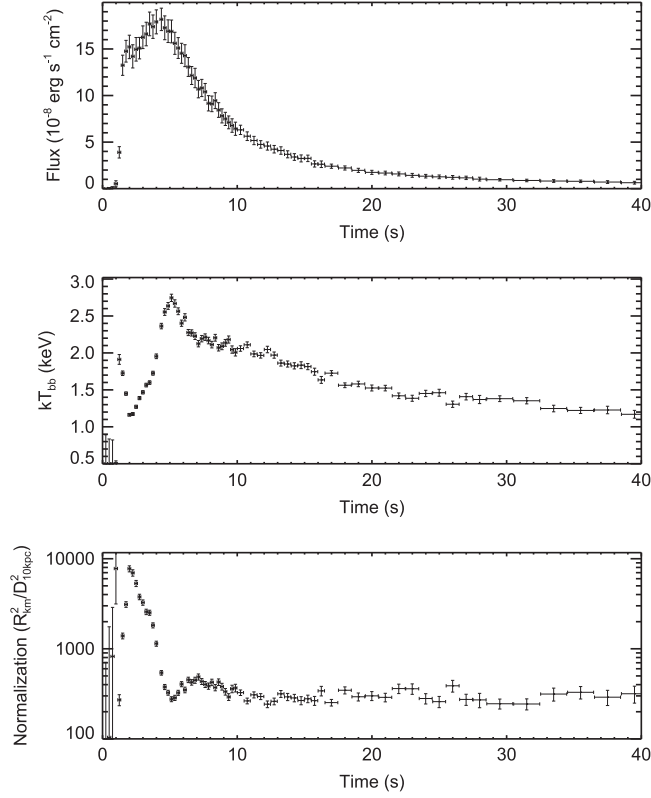
Figure 18. Evolution of the bolometric flux (top), color temperature (middle), and the blackbody normalization (bottom) of burst 32 obtained from the spectral fits.
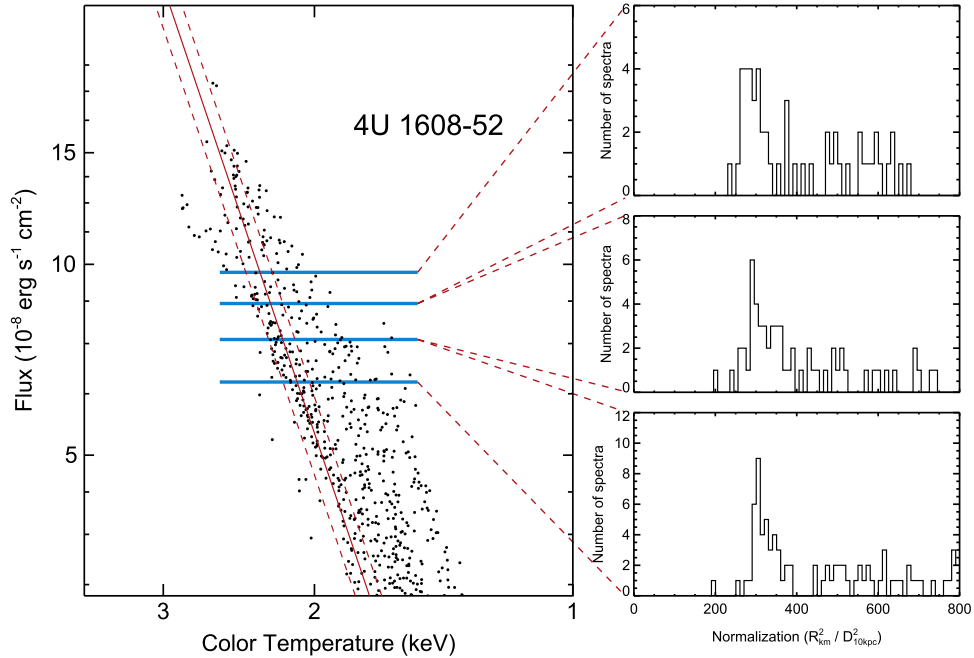

Figure 19. The evolution of the flux and temperature measured for all the spectra in the cooling tails of bursts from 4U 1608−52. The diagonal lines show the best-fit blackbody normalization and its 1σ uncertainty. The histograms at three different flux levels visually identify the main apparent angular size track and the outliers.

To determine the apparent angular size that we use in the radius measurements, we combined all of the data in the cooling tails of the X-ray bursts from 4U 1608−52, including burst 32, using the methods described in Güver et al. (2012b). We used the Bayesian Gaussian-mixture model to determine the signal and the outliers and Bayesian technique to infer the width of the distribution. We show in Figure 19 the data points along with three representative histograms of the blackbody normalization at three different flux bins. Despite the scatter in the outliers, the main cooling track is clearly seen in these plots. We finally assigned the width that we

Table 5
Posterior Likelihoods over the Observed Parameters of the Burst Sources

Source	App. Angular Size (km/10 kpc)^2	Touchdown Flux (10^{-8} erg s^{-1} cm^{-2})	Distance (kpc)
4U 1820−30	97.6 ± 11.2	5.22 ± 0.44	7.47 ± 0.38
SAX J1748.9−2021	91.8 ± 8.4	3.74 ± 0.46	8.01 ± 0.47
EXO 1745−248	129.8 ± 15.0	6.21 ± 0.65	6.08 ± 0.40
KS 1731−260	97.2 ± 7.5	4.48 ± 0.47	6.77 ± 0.75
4U 1724−207	121.1 ± 11.9	4.95 ± 0.50	7.27 ± 0.37
4U 1608−52	333.4 ± 36.8	16.9 ± 1.78	3.63 ± 0.29

found from the Bayesian analysis as the systematic uncertainty in the apparent angular size, which we found to be 314 ± 44.3 (km/kpc)^2 (see Table 1).

Because it is a PRE event, we also included burst 32 in the determination of the touchdown flux and the touchdown temperature for 4U 1608−52 (see the upper right panel of Figure 8 and Table 1).

A.3. Bursts Used in the Analysis

In Table 4, we list the IDs of the bursts we used in the determination of the touchdown flux and the apparent angular size for each source.

A.4. The Posterior Likelihoods over the Observed Parameters of Burst Sources

We report in Table 5 the posterior likelihoods over each of the three measured quantities for the six sources that show thermonuclear bursts. The central values of the posterior likelihoods are always within the 68% range of the prior likelihoods shown in Table 1, indicating a high degree of consistency between the measurements that are used to infer the neutron star radii.

REFERENCES

Akmal, A., Pandharipande, V. R., & Ravenhall, D. G. 1998, PhRvC, 58, 1804
Altamirano, D., Casella, P., Patruno, A., Wijnands, R., & van der Klis, M. 2008, ApJL, 674, L45
Antoniadis, J., Freire, P. C. C., Wex, N., et al. 2013, Sci, 340, 448
Bauböck, M., Özel, F., Psaltis, D., & Morsink, S. M. 2015, ApJ, 799, 22
Bauböck, M., Psaltis, D., Özel, F., & Johannsen, T. 2012, ApJ, 753, 175
Bludman, S. A., & Ruderman, M. A. 1968, PhRv, 170, 1176
Brown, E. F., Bildsten, L., & Rutledge, R. E. 1998, ApJL, 504, L95
Cardelli, J. A., Clayton, G. C., & Mathis, J. S. 1989, ApJ, 345, 245
Carretta, E., Gratton, R. G., Clementini, G., & Fusi Pecci, F. 2000, ApJ, 533, 215
Demorest, P. B., Pennucci, T., Ransom, S. M., Roberts, M. S. E., & Hessels, J. W. T. 2010, Natur, 467, 1081
Doe, S., Nguyen, D., Stawarz, C., et al. 2007, adass XVI, 376, 543
Douchin, F., & Haensel, P. 2001, A&A, 380, 151
Ellis, G. F. R., Maartens, R., & MacCallum, M. A. H. 2007, GReGr, 39, 1651
Foight, D., Güver, T., Slane, P., & Özel, F. 2015, ApJ, submitted (arXiv:1504.07274)
Freeman, P., Doe, S., & Siemiginowska, A. 2001, Proc. SPIE, 4477, 76
Galloway, D. K., Muno, M. P., Hartman, J. M., Psaltis, D., & Chakrabarty, D. 2008a, ApJS, 179, 360
Galloway, D. K., Özel, F., & Psaltis, D. 2008b, MNRAS, 387, 268
Gandolfi, S., Carlson, J., & Reddy, S. 2012, PhRvC, 85, 032801
Guillot, S., Brown, E. F., & Rutledge, R. E. 2011, ApJ, 732, 88
Guillot, S., & Rutledge, R. E. 2014, ApJL, 796, LL3
Guillot, S., Servillat, M., Webb, N. A., & Rutledge, R. E. 2013, ApJ, 772, 7
Güver, T., & Özel, F. 2009, MNRAS, 400, 2050
Güver, T., & Özel, F. 2013, ApJL, 765, LL1
Güver, T., Özel, F., Cabrera-Lavers, A., & Wroblewski, P. 2010a, ApJ, 712, 964
Güver, T., Özel, F., Marshall, H., et al. 2015, ApJ, submitted (arXiv:1501.05330)
Güver, T., Özel, F., & Psaltis, D. 2012a, ApJ, 747, 77
Güver, T., Psaltis, D., & Özel, F. 2012b, ApJ, 747, 76
Güver, T., Wroblewski, P., Camarota, L., & Özel, F. 2010b, ApJ, 719, 1807
Harris, W. E. 1996, AJ, 112, 1487
Hartman, J. M., Chakrabarty, D., Galloway, D. K., et al. 2003, BAAS, 35, 865
Hebeler, K., Lattimer, J. M., & Pethick, C. J. 2010, PhRvL, 105, 161102

Heinke, C. O., Cohn, H. N., Lugger, P. M., et al. 2014, MNRAS, 444, 443
Heinke, C. O., Edmonds, P. D., Grindlay, J. E., et al. 2003, ApJ, 590, 809
Heinke, C. O., Rybicki, G. B., Narayan, R., & Grindlay, J. E. 2006, ApJ, 644, 1090
Huenemoerder, D. P., Mitschang, A., Dewey, D., et al. 2011, AJ, 141, 129
in 't Zand, J. J. M., & Weinberg, N. N. 2010, A&A, 520, A81
Kajava, J. J. E., Nättilä, J., Latvala, O.-M., et al. 2014, MNRAS, 445, 4218
Kojo, T., Powell, P. D., Song, Y., & Baym, G. 2015, PhRvD, 91, 045003
Kuulkers, E., den Hartog, P. R., in 't Zand, J. M. M., et al. 2003, A&A, 399, 663
Lattimer, J. M., & Prakash, M. 2001, ApJ, 550, 426
Lattimer, J. M., & Prakash, M. 2010, arXiv:1012.3208
Lattimer, J. M., & Steiner, A. W. 2014a, ApJ, 784, 123
Lattimer, J. M., & Steiner, A. W. 2014b, EPJA, 50, 40
Lindblom, L. 1992, ApJ, 398, 569
London, R. A., Taam, R. E., & Howard, W. M. 1986, ApJ, 306, 170
Lugger, P. M., Cohn, H. N., Heinke, C. O., Grindlay, J. E., & Edmonds, P. D. 2007, ApJ, 657, 286
Madej, J., Joss, P. C., & Różańska, A. 2004, ApJ, 602, 904
Majczyna, A., Madej, J., Joss, P. C., & Różańska, A. 2005, A&A, 430, 643
Miller, J. M., Cackett, E. M., & Reis, R. C. 2009, ApJL, 707, L77
Morales, J., Pandharipande, V. R., & Ravenhall, D. G. 2002, PhRvC, 66, 054308
Morrison, R., & McCammon, D. 1983, ApJ, 270, 119
Ortolani, S., Barbuy, B., Bica, E., Zoccali, M., & Renzini, A. 2007, A&A, 470, 1043
Özel, F. 2013, RPPh, 76, 016901
Özel, F., Baym, G., & Güver, T. 2010, PhRvD, 82, 101301
Özel, F., Gould, A., & Güver, T. 2012a, ApJ, 748, 5
Özel, F., Güver, T., & Psaltis, D. 2009, ApJ, 693, 1775
Özel, F., & Psaltis, D. 2009, PhRvD, 80, 103003
Özel, F., Psaltis, D., & Güver, T. 2015, ApJ, submitted (arXiv:1509.02924)
Özel, F., Psaltis, D., Narayan, R., & Santos Villarreal, A. 2012b, ApJ, 757, 55
Paczynski, B. 1983, ApJ, 267, 315
Pieper, S. C., Pandharipande, V. R., Wiringa, R. B., & Carlson, J. 2001, PhRvC, 64, 014001
Poutanen, J., Nättilä, J., Kajava, J. J. E., et al. 2014, MNRAS, 442, 3777
Racine, R., & Harris, W. E. 1989, AJ, 98, 1609
Read, J. S., Lackey, B. D., Owen, B. J., & Friedman, J. L. 2009, PhRvD, 79, 124032

Reid, M. J. 1993, ARA&A, 31, 345
Servillat, M., Heinke, C. O., Ho, W. C. G., et al. 2012, MNRAS, 423, 1556
Smith, D. A., Morgan, E. H., & Bradt, H. 1997, ApJL, 479, L137
Steiner, A. W., Lattimer, J. M., & Brown, E. F. 2010, ApJ, 722, 33
Steiner, A. W., Lattimer, J. M., & Brown, E. F. 2013, ApJL, 765, L5
Stella, L., White, N. E., & Priedhorsky, W. 1987, ApJL, 315, L49
Suleimanov, V., Poutanen, J., & Werner, K. 2011, A&A, 527, AA139
Suleimanov, V., Poutanen, J., & Werner, K. 2012, A&A, 545, AA120

Valenti, E., Ferraro, F. R., & Origlia, L. 2007, AJ, 133, 1287
Valenti, E., Ferraro, F. R., & Origlia, L. 2010, MNRAS, 402, 1729
Watkins, L. L., van de Ven, G., den Brok, M., & van den Bosch, R. C. E. 2013, MNRAS, 436, 2598
Webb, N. A., & Barret, D. 2007, ApJ, 671, 727
Wilms, J., Allen, A., & McCray, R. 2000, ApJ, 542, 914
Zurita, C., Kuulkers, E., Bandyopadhyay, R. M., et al. 2010, A&A, 512, A26